FERMILAB-PUB-05-220-E

Measurement of the $t\bar{t}$ Production Cross Section in $p\bar{p}$ Collisions at $\sqrt{s} = 1.96$ TeV Using Lepton Plus Jets Events with Semileptonic B Decays to Muons

D. Acosta,[16] J. Adelman,[12] T. Affolder,[9] T. Akimoto,[54] M.G. Albrow,[15] D. Ambrose,[15] S. Amerio,[42] D. Amidei,[33] A. Anastassov,[50] K. Anikeev,[15] A. Annovi,[44] J. Antos,[1] M. Aoki,[54] G. Apollinari,[15] T. Arisawa,[56] J-F. Arguin,[32] A. Artikov,[13] W. Ashmanskas,[15] A. Attal,[7] F. Azfar,[41] P. Azzi-Bacchetta,[42] N. Bacchetta,[42] H. Bachacou,[28] W. Badgett,[15] A. Barbaro-Galtieri,[28] G.J. Barker,[25] V.E. Barnes,[46] B.A. Barnett,[24] S. Baroiant,[6] G. Bauer,[31] F. Bedeschi,[44] S. Behari,[24] S. Belforte,[53] G. Bellettini,[44] J. Bellinger,[58] A. Belloni,[31] E. Ben-Haim,[15] D. Benjamin,[14] A. Beretvas,[15] T. Berry,[29] A. Bhatti,[48] M. Binkley,[15] D. Bisello,[42] M. Bishai,[15] R.E. Blair,[2] C. Blocker,[5] K. Bloom,[33] B. Blumenfeld,[24] A. Bocci,[48] A. Bodek,[47] G. Bolla,[46] A. Bolshov,[31] D. Bortoletto,[46] J. Boudreau,[45] S. Bourov,[15] B. Brau,[9] C. Bromberg,[34] E. Brubaker,[12] J. Budagov,[13] H.S. Budd,[47] K. Burkett,[15] G. Busetto,[42] P. Bussey,[19] K.L. Byrum,[2] S. Cabrera,[14] M. Campanelli,[18] M. Campbell,[33] F. Canelli,[7] A. Canepa,[46] M. Casarsa,[53] D. Carlsmith,[58] R. Carosi,[44] S. Carron,[14] M. Cavalli-Sforza,[3] A. Castro,[4] P. Catastini,[44] D. Cauz,[53] A. Cerri,[28] L. Cerrito,[41] J. Chapman,[33] Y.C. Chen,[1] M. Chertok,[6] G. Chiarelli,[44] G. Chlachidze,[13] F. Chlebana,[15] I. Cho,[27] K. Cho,[27] D. Chokheli,[13] J.P. Chou,[20] S. Chuang,[58] K. Chung,[11] W-H. Chung,[58] Y.S. Chung,[47] M. Cijliak,[44] C.I. Ciobanu,[23] M.A. Ciocci,[44] A.G. Clark,[18] D. Clark,[5] M. Coca,[14] A. Connolly,[28] M. Convery,[48] J. Conway,[6] B. Cooper,[30] K. Copic,[33] M. Cordelli,[17] G. Cortiana,[42] J. Cranshaw,[52] J. Cuevas,[10] A. Cruz,[16] R. Culbertson,[15] C. Currat,[28] D. Cyr,[58] D. Dagenhart,[5] S. Da Ronco,[42] S. D'Auria,[19] P. de Barbaro,[47] S. De Cecco,[49] A. Deisher,[28] G. De Lentdecker,[47] M. Dell'Orso,[44] S. Demers,[47] L. Demortier,[48] M. Deninno,[4] D. De Pedis,[49] P.F. Derwent,[15] C. Dionisi,[49] J.R. Dittmann,[15] P. DiTuro,[50] C. Dörr,[25] A. Dominguez,[28] S. Donati,[44] M. Donega,[18] J. Donini,[42] M. D'Onofrio,[18] T. Dorigo,[42] K. Ebina,[56] J. Efron,[38] J. Ehlers,[18] R. Erbacher,[6] M. Erdmann,[25] D. Errede,[23] S. Errede,[23] R. Eusebi,[47] H-C. Fang,[28] S. Farrington,[29] I. Fedorko,[44] W.T. Fedorko,[12] R.G. Feild,[59] M. Feindt,[25] J.P. Fernandez,[46] R.D. Field,[16] G. Flanagan,[34] L.R. Flores-Castillo,[45] A. Foland,[20] S. Forrester,[6] G.W. Foster,[15] M. Franklin,[20] J.C. Freeman,[28] Y. Fujii,[26] I. Furic,[12] A. Gajjar,[29] M. Gallinaro,[48] J. Galyardt,[11] M. Garcia-Sciveres,[28] A.F. Garfinkel,[46] C. Gay,[59] H. Gerberich,[14] D.W. Gerdes,[33] E. Gerchtein,[11] S. Giagu,[49] P. Giannetti,[44] A. Gibson,[28] K. Gibson,[11] C. Ginsburg,[15] K. Giolo,[46] M. Giordani,[53] M. Giunta,[44] G. Giurgiu,[11] V. Glagolev,[13] D. Glenzinski,[15] M. Gold,[36] N. Goldschmidt,[33] D. Goldstein,[7] J. Goldstein,[41] G. Gomez,[10] G. Gomez-Ceballos,[10] M. Goncharov,[51] O. González,[46] I. Gorelov,[36] A.T. Goshaw,[14] Y. Gotra,[45] K. Goulianos,[48] A. Gresele,[42] M. Griffiths,[29] C. Grosso-Pilcher,[12] U. Grundler,[23] J. Guimaraes da Costa,[20] C. Haber,[28] K. Hahn,[43] S.R. Hahn,[15] E. Halkiadakis,[47] A. Hamilton,[32] B-Y. Han,[47] R. Handler,[58] F. Happacher,[17] K. Hara,[54] M. Hare,[55] R.F. Harr,[57] R.M. Harris,[15] F. Hartmann,[25] K. Hatakeyama,[48] J. Hauser,[7] C. Hays,[14] H. Hayward,[29] B. Heinemann,[29] J. Heinrich,[43] M. Hennecke,[25] M. Herndon,[24] C. Hill,[9] D. Hirschbuehl,[25] A. Hocker,[15] K.D. Hoffman,[12] A. Holloway,[20] S. Hou,[1] M.A. Houlden,[29] B.T. Huffman,[41] Y. Huang,[14] R.E. Hughes,[38] J. Huston,[34] K. Ikado,[56] J. Incandela,[9] G. Introzzi,[44] M. Iori,[49] Y. Ishizawa,[54] C. Issever,[9] A. Ivanov,[6] Y. Iwata,[22] B. Iyutin,[31] E. James,[15] D. Jang,[50] B. Jayatilaka,[33] D. Jeans,[49] H. Jensen,[15] E.J. Jeon,[27] M. Jones,[46] K.K. Joo,[27] S.Y. Jun,[11] T. Junk,[23] T. Kamon,[51] J. Kang,[33] M. Karagoz Unel,[37] P.E. Karchin,[57] Y. Kato,[40] Y. Kemp,[25] R. Kephart,[15] U. Kerzel,[25] V. Khotilovich,[51] B. Kilminster,[38] D.H. Kim,[27] H.S. Kim,[23] J.E. Kim,[27] M.J. Kim,[11] M.S. Kim,[27] S.B. Kim,[27] S.H. Kim,[54] Y.K. Kim,[12] M. Kirby,[14] L. Kirsch,[5] S. Klimenko,[16] M. Klute,[31] B. Knuteson,[31] B.R. Ko,[14] H. Kobayashi,[54] D.J. Kong,[27] K. Kondo,[56] J. Konigsberg,[16] K. Kordas,[32] A. Korn,[31] A. Korytov,[16] A.V. Kotwal,[14] A. Kovalev,[43] J. Kraus,[23] I. Kravchenko,[31] A. Kreymer,[15] J. Kroll,[43] M. Kruse,[14] V. Krutelyov,[51] S.E. Kuhlmann,[2] S. Kwang,[12] A.T. Laasanen,[46] S. Lai,[32] S. Lami,[44] S. Lammel,[15] M. Lancaster,[30] R. Lander,[6] K. Lannon,[38] A. Lath,[50] G. Latino,[44] I. Lazzizzera,[42] C. Lecci,[25] T. LeCompte,[2] J. Lee,[27] J. Lee,[47] S.W. Lee,[51] R. Lefèvre,[3] N. Leonardo,[31] S. Leone,[44] S. Levy,[12] J.D. Lewis,[15] K. Li,[59] C. Lin,[59] C.S. Lin,[15] M. Lindgren,[15] E. Lipeles,[8] T.M. Liss,[23] A. Lister,[18] D.O. Litvintsev,[15] T. Liu,[15] Y. Liu,[18] N.S. Lockyer,[43] A. Loginov,[35] M. Loreti,[42] P. Loverre,[49] R-S. Lu,[1] D. Lucchesi,[42] P. Lujan,[28] P. Lukens,[15] G. Lungu,[16] L. Lyons,[41] J. Lys,[28] R. Lysak,[1] E. Lytken,[46] D. MacQueen,[32] R. Madrak,[15] K. Maeshima,[15] P. Maksimovic,[24] G. Manca,[29] Margaroli,[4] R. Marginean,[15] C. Marino,[23] A. Martin,[59] M. Martin,[24] V. Martin,[37] M. Martínez,[3] T. Maruyama,[54] H. Matsunaga,[54] M. Mattson,[57] P. Mazzanti,[4] K.S. McFarland,[47] D. McGivern,[30] P.M. McIntyre,[51] P. McNamara,[50] McNulty,[29] A. Mehta,[29] S. Menzemer,[31] A. Menzione,[44] P. Merkel,[46]

C. Mesropian,[48] A. Messina,[49] T. Miao,[15] N. Miladinovic,[5] J. Miles,[31] L. Miller,[20] R. Miller,[34] J.S. Miller,[33] C. Mills,[9] R. Miquel,[28] S. Miscetti,[17] G. Mitselmakher,[16] A. Miyamoto,[26] N. Moggi,[4] B. Mohr,[7] R. Moore,[15] M. Morello,[44] P.A. Movilla Fernandez,[28] J. Muelmenstaedt,[28] A. Mukherjee,[15] M. Mulhearn,[31] T. Muller,[25] R. Mumford,[24] A. Munar,[43] P. Murat,[15] J. Nachtman,[15] S. Nahn,[59] I. Nakano,[39] A. Napier,[55] R. Napora,[24] D. Naumov,[36] V. Necula,[16] T. Nelson,[15] C. Neu,[43] M.S. Neubauer,[8] J. Nielsen,[28] T. Nigmanov,[45] L. Nodulman,[2] O. Norniella,[3] T. Ogawa,[56] S.H. Oh,[14] Y.D. Oh,[27] T. Ohsugi,[22] T. Okusawa,[40] R. Oldeman,[29] R. Orava,[21] W. Orejudos,[28] K. Osterberg,[21] C. Pagliarone,[44] E. Palencia,[10] R. Paoletti,[44] V. Papadimitriou,[15] A.A. Paramonov,[12] S. Pashapour,[32] J. Patrick,[15] G. Pauletta,[53] M. Paulini,[11] C. Paus,[31] D. Pellett,[6] A. Penzo,[53] T.J. Phillips,[14] G. Piacentino,[44] J. Piedra,[10] K.T. Pitts,[23] C. Plager,[7] L. Pondrom,[58] G. Pope,[45] X. Portell,[3] O. Poukhov,[13] N. Pounder,[41] F. Prakoshyn,[13] A. Pronko,[16] J. Proudfoot,[2] F. Ptohos,[17] G. Punzi,[44] J. Rademacker,[41] M.A. Rahaman,[45] A. Rakitine,[31] S. Rappoccio,[20] F. Ratnikov,[50] H. Ray,[33] B. Reisert,[15] V. Rekovic,[36] P. Renton,[41] M. Resigno,[49] F. Rimondi,[4] K. Rinnert,[25] L. Ristori,[44] W.J. Robertson,[14] A. Robson,[19] T. Rodrigo,[10] S. Rolli,[55] R. Roser,[15] R. Rossin,[16] C. Rott,[46] J. Russ,[11] V. Rusu,[12] A. Ruiz,[10] D. Ryan,[55] H. Saarikko,[21] S. Sabik,[32] A. Safonov,[6] R. St. Denis,[19] W.K. Sakumoto,[47] G. Salamanna,[49] D. Saltzberg,[7] C. Sanchez,[3] L. Santi,[53] S. Sarkar,[49] K. Sato,[54] P. Savard,[32] A. Savoy-Navarro,[15] P. Schlabach,[15] E.E. Schmidt,[15] M.P. Schmidt,[59] M. Schmitt,[37] T. Schwarz,[33] L. Scodellaro,[10] A.L. Scott,[9] A. Scribano,[44] F. Scuri,[44] A. Sedov,[46] S. Seidel,[36] Y. Seiya,[40] A. Semenov,[13] F. Semeria,[4] L. Sexton-Kennedy,[15] I. Sfiligoi,[17] M.D. Shapiro,[28] T. Shears,[29] P.F. Shepard,[45] D. Sherman,[20] M. Shimojima,[54] M. Shochet,[12] Y. Shon,[58] I. Shreyber,[35] A. Sidoti,[44] A. Sill,[52] P. Sinervo,[32] A. Sisakyan,[13] J. Sjolin,[41] A. Skiba,[25] A.J. Slaughter,[15] K. Sliwa,[55] D. Smirnov,[36] J.R. Smith,[6] F.D. Snider,[15] R. Snihur,[32] M. Soderberg,[33] A. Soha,[6] S.V. Somalwar,[50] J. Spalding,[15] M. Spezziga,[52] F. Spinella,[44] P. Squillacioti,[44] H. Stadie,[25] M. Stanitzki,[59] B. Stelzer,[32] O. Stelzer-Chilton,[32] D. Stentz,[37] J. Strologas,[36] D. Stuart,[9] J. S. Suh,[27] A. Sukhanov,[16] K. Sumorok,[31] H. Sun,[55] T. Suzuki,[54] A. Taffard,[23] R. Tafirout,[32] H. Takano,[54] R. Takashima,[39] Y. Takeuchi,[54] K. Takikawa,[54] M. Tanaka,[2] R. Tanaka,[39] N. Tanimoto,[39] M. Tecchio,[33] P.K. Teng,[1] K. Terashi,[48] R.J. Tesarek,[15] S. Tether,[31] J. Thom,[15] A.S. Thompson,[19] E. Thomson,[43] P. Tipton,[47] V. Tiwari,[11] S. Tkaczyk,[15] D. Toback,[51] K. Tollefson,[34] T. Tomura,[54] D. Tonelli,[44] M. Tönnesmann,[34] S. Torre,[44] D. Torretta,[15] S. Tourneur,[15] W. Trischuk,[32] R. Tsuchiya,[56] S. Tsuno,[39] D. Tsybychev,[16] N. Turini,[44] F. Ukegawa,[54] T. Unverhau,[19] S. Uozumi,[54] D. Usynin,[43] L. Vacavant,[28] A. Vaiciulis,[47] A. Varganov,[33] S. Vejcik III,[15] G. Velev,[15] V. Veszpremi,[46] G. Veramendi,[23] T. Vickey,[23] R. Vidal,[15] I. Vila,[10] R. Vilar,[10] I. Vollrath,[32] I. Volobouev,[28] M. von der Mey,[7] P. Wagner,[51] R.G. Wagner,[2] R.L. Wagner,[15] W. Wagner,[25] R. Wallny,[7] T. Walter,[25] Z. Wan,[50] M.J. Wang,[1] S.M. Wang,[16] A. Warburton,[32] B. Ward,[19] S. Waschke,[19] D. Waters,[30] T. Watts,[50] M. Weber,[28] W.C. Wester III,[15] B. Whitehouse,[55] D. Whiteson,[43] A.B. Wicklund,[2] E. Wicklund,[15] H.H. Williams,[43] P. Wilson,[15] B.L. Winer,[38] P. Wittich,[43] S. Wolbers,[15] C. Wolfe,[12] M. Wolter,[55] M. Worcester,[7] S. Worm,[50] T. Wright,[33] X. Wu,[18] F. Würthwein,[8] A. Wyatt,[30] A. Yagil,[15] T. Yamashita,[39] K. Yamamoto,[40] J. Yamaoka,[50] C. Yang,[59] U.K. Yang,[12] W. Yao,[28] G.P. Yeh,[15] J. Yoh,[15] K. Yorita,[56] T. Yoshida,[40] I. Yu,[27] S. Yu,[43] J.C. Yun,[15] L. Zanello,[49] A. Zanetti,[53] I. Zaw,[20] F. Zetti,[44] J. Zhou,[50] and S. Zucchelli[4]

(CDF Collaboration)

[1] *Institute of Physics, Academia Sinica, Taipei, Taiwan 11529,Republic of China*
[2] *Argonne National Laboratory, Argonne, Illinois 60439*
[3] *Institut de Fisica d'Altes Energies, Universitat Autonoma de Barcelona, E-08193, Bellaterra (Barcelona), Spain*
[4] *Istituto Nazionale di Fisica Nucleare, University of Bologna, I-40127 Bologna, Italy*
[5] *Brandeis University, Waltham, Massachusetts 02254*
[6] *University of California, Davis, Davis, California 95616*
[7] *University of California, Los Angeles, Los Angeles, California 90024*
[8] *University of California, San Diego, La Jolla, California 92093*
[9] *University of California, Santa Barbara, Santa Barbara, California 93106*
[10] *Instituto de Fisica de Cantabria, CSIC-University of Cantabria, 39005 Santander, Spain*
[11] *Carnegie Mellon University, Pittsburgh, PA 15213*
[12] *Enrico Fermi Institute, University of Chicago, Chicago, Illinois 60637*
[13] *Joint Institute for Nuclear Research, RU-141980 Dubna, Russia*
[14] *Duke University, Durham, North Carolina 27708*
[15] *Fermi National Accelerator Laboratory, Batavia, Illinois 60510*
[16] *University of Florida, Gainesville, Florida 32611*
[17] *Laboratori Nazionali di Frascati, Istituto Nazionale di Fisica Nucleare, I-00044 Frascati, Italy*
[18] *University of Geneva, CH-1211 Geneva 4, Switzerland*
[19] *Glasgow University, Glasgow G12 8QQ, United Kingdom*
[20] *Harvard University, Cambridge, Massachusetts 02138*

[21] Division of High Energy Physics, Department of Physics,
University of Helsinki and Helsinki Institute of Physics, FIN-00014, Helsinki, Finland
[22] Hiroshima University, Higashi-Hiroshima 724, Japan
[23] University of Illinois, Urbana, Illinois 61801
[24] The Johns Hopkins University, Baltimore, Maryland 21218
[25] Institut für Experimentelle Kernphysik, Universität Karlsruhe, 76128 Karlsruhe, Germany
[26] High Energy Accelerator Research Organization (KEK), Tsukuba, Ibaraki 305, Japan
[27] Center for High Energy Physics: Kyungpook National University, Taegu 702-701; Seoul National University,
Seoul 151-742; and SungKyunKwan University, Suwon 440-746; Korea
[28] Ernest Orlando Lawrence Berkeley National Laboratory, Berkeley, California 94720
[29] University of Liverpool, Liverpool L69 7ZE, United Kingdom
[30] University College London, London WC1E 6BT, United Kingdom
[31] Massachusetts Institute of Technology, Cambridge, Massachusetts 02139
[32] Institute of Particle Physics: McGill University, Montréal,
Canada H3A 2T8; and University of Toronto, Toronto, Canada M5S 1A7
[33] University of Michigan, Ann Arbor, Michigan 48109
[34] Michigan State University, East Lansing, Michigan 48824
[35] Institution for Theoretical and Experimental Physics, ITEP, Moscow 117259, Russia
[36] University of New Mexico, Albuquerque, New Mexico 87131
[37] Northwestern University, Evanston, Illinois 60208
[38] The Ohio State University, Columbus, Ohio 43210
[39] Okayama University, Okayama 700-8530, Japan
[40] Osaka City University, Osaka 588, Japan
[41] University of Oxford, Oxford OX1 3RH, United Kingdom
[42] University of Padova, Istituto Nazionale di Fisica Nucleare,
Sezione di Padova-Trento, I-35131 Padova, Italy
[43] University of Pennsylvania, Philadelphia, Pennsylvania 19104
[44] Istituto Nazionale di Fisica Nucleare Pisa, Universities of Pisa,
Siena and Scuola Normale Superiore, I-56127 Pisa, Italy
[45] University of Pittsburgh, Pittsburgh, Pennsylvania 15260
[46] Purdue University, West Lafayette, Indiana 47907
[47] University of Rochester, Rochester, New York 14627
[48] The Rockefeller University, New York, New York 10021
[49] Istituto Nazionale di Fisica Nucleare, Sezione di Roma 1,
University di Roma "La Sapienza," I-00185 Roma, Italy
[50] Rutgers University, Piscataway, New Jersey 08855
[51] Texas A&M University, College Station, Texas 77843
[52] Texas Tech University, Lubbock, Texas 79409
[53] Istituto Nazionale di Fisica Nucleare, University of Trieste/ Udine, Italy
[54] University of Tsukuba, Tsukuba, Ibaraki 305, Japan
[55] Tufts University, Medford, Massachusetts 02155
[56] Waseda University, Tokyo 169, Japan
[57] Wayne State University, Detroit, Michigan 48201
[58] University of Wisconsin, Madison, Wisconsin 53706
[59] Yale University, New Haven, Connecticut 06520

(Dated: June 2, 2005)

We present a measurement of the $t\bar{t}$ production cross section using $194\,\mathrm{pb}^{-1}$ of CDF II data using events with a high transverse momentum electron or muon, three or more jets, and missing transverse energy. The measurement assumes 100% $t \to Wb$ branching fraction. Events consistent with $t\bar{t}$ decay are found by identifying jets containing heavy flavor semileptonic decays to muons. The dominant backgrounds are evaluated directly from the data. Based on 20 candidate events and an expected background of 9.5 ± 1.1 events, we measure a production cross section of $5.3 \pm 3.3^{+1.3}_{-1.0}$ pb, in agreement with the standard model.

PACS numbers: 13.85Ni, 13.85Qk, 14.65Ha

I. INTRODUCTION

Top quark pair production in the standard model proceeds via either quark-antiquark annihilation or gluon-gluon fusion. At the Fermilab Tevatron collider, with a center-of-mass energy of 1.96 TeV, quark-antiquark annihilation is

expected to dominate. For a top mass of 175 GeV/c^2, the calculated cross section is $6.7^{+0.7}_{-0.9}$ pb [1], and is approximately 0.2 pb smaller for each 1 GeV/c^2 increase in the value of the top mass over the range 170 GeV/c^2 $< M_{\rm top} <$ 190 GeV/c^2.

Measurements of the cross section for top quark pair production provide a test of QCD, as well as the standard model decay $t \to Wb$. Non-standard model production mechanisms, such as the production and decay of a heavy resonance into $t\bar{t}$ pairs [2], could enhance the measured cross section. Non-standard model top quark decays, such as the decay into supersymmetric particles [3], could suppress the measured value, for which a $t \to Wb$ branching fraction of nearly 100% is assumed.

In this paper we report a measurement of the $t\bar{t}$ production cross section in $p\bar{p}$ collisions at $\sqrt{s} = 1.96$ TeV with the CDF II detector at the Fermilab Tevatron. The standard model decay $t \to Wb$ of the top quark results in a final state from $t\bar{t}$ production of two W bosons and two bottom quarks. We select events consistent with a decay of one of the W bosons to an electron or muon plus a neutrino, both of which have large momentum transverse to the beam direction ($P_{\rm T}$). We refer to these high $P_{\rm T}$ electrons or muons as the "primary lepton". The neutrino is undetected and results in an imbalance in transverse momentum. The imbalance is labeled "missing $E_{\rm T}$" ($\not\!\!E_T$) since it is reconstructed based on the flow of energy in the calorimeter [4]. The other W boson in the event decays to a pair of quarks. The two quarks from the W boson and the two b quarks from the top decays hadronize and are observed as jets of charged and neutral particles. This mode is referred as W plus jets. We take advantage of the semileptonic decay of b hadrons to muons to identify final-state jets that result from hadronization of the bottom quarks. Such a technique, called "soft-lepton tagging" (SLT), is effective in reducing the background to the $t\bar{t}$ signal from W boson produced in association with several hadronic jets with large transverse momentum. The production cross section is measured in events with three or more jets and at least one SLT tagged jet.

This measurement is complementary to other measurements from CDF II, which use secondary vertex tagging, kinematic fitting, or a combination of the two [5] [6] [7]. A forthcoming paper [8] will present a combined cross section measurement based on the result of these four analyses.

Previous measurements [9] from Run I at the Tevatron have measured a production cross sections statistically consistent with the standard model prediction. This and other Run II measurements are made at a slightly higher center of mass energy (1.96 TeV vs. 1.8 TeV) and with nearly twice as much integrated luminosity.

The organization of this paper is as follows: Section II reviews the detector systems relevant to this analysis. The trigger and event selection, the data and the Monte Carlo samples and the SLT tagging algorithm are described in Section III. The estimate of the background is presented in Section IV. The acceptance and the $t\bar{t}$ event tagging efficiency are described in Section V. The evaluation of the systematic uncertainties on the measurement is presented in Section VI. The $t\bar{t}$ production cross section measurement and the conclusions are presented in Section VII and Section VIII.

II. THE CDF II DETECTOR

The CDF II detector is described in detail in [10], only the components relevant to this measurement are summarized here. The CDF II detector is a nearly azimuthally and forward-backward symmetric detector designed to study $p\bar{p}$ interactions at the Fermilab Tevatron. It consists of a magnetic spectrometer surrounded by calorimeters and muon chambers. An elevation view of the CDF II detector is shown in Figure 1.

Charged particles are tracked inside a 1.4 T solenoidal magnetic field by an 8-layer silicon strip detector covering radii from 1.5 cm to 28 cm, followed by the central outer tracker (COT), an open-cell drift chamber that provides up to 96 measurements of charged particle position over the radial region from 40 cm to 137 cm. The 96 COT measurements are arranged in 8 "superlayers" of 12 sense wires each alternating between axial and 2° stereo. The COT and the silicon detectors track charged particles for $|\eta| < 1$ and $|\eta| < 2$, respectively.

Surrounding the tracking system are electromagnetic and hadronic calorimeters, used to measure charged and neutral particle energies. The electromagnetic calorimeter is a lead-scintillator sandwich and the hadronic calorimeter is an iron-scintillator sandwich. Both calorimeters are segmented in azimuth and polar angle to provide directional information for the energy deposition. The segmentation varies with position on the detector and is 15° in azimuth by 0.1 units of η in the central region ($|\eta| < 1.1$). Segmentation in the plug region ($1.1 < |\eta| < 3.6$) is 7.5° up to $|\eta| < 2.1$, and 15° for $|\eta| > 2.1$ in azimuth, while ranging from 0.1 to 0.64 units of η in pseudo-rapidity (a nearly constant 2.7° change in polar angle). The electromagnetic calorimeters are instrumented with proportional and scintillating strip detectors that measure the transverse profile of electromagnetic showers at a depth corresponding to the shower maximum.

Outside the central calorimeter are four layers of muon drift chambers covering $|\eta| < 0.6$ (CMU). The calorimeter provides approximately 1 meter of steel shielding. Behind an additional 60 cm of steel in the central region sit an additional four layers of muon drift chambers (CMP) arranged in a box-shaped layout around the central detector. Central muon extension (CMX) chambers, which are arrayed in a conical geometry, provide muon detection for the

region $0.6 < |\eta| < 1$ with four to eight layers of drift chambers, depending on polar angle. All the muon chambers measure the coordinates of hits in the drift direction, x, via a drift time measurement and a calibrated drift velocity. The CMU and the CMX also measure the longitudinal coordinate, z. The longitudinal coordinate is measured in the CMU by comparing the height of pulses, encoded in time-over-threshold, at opposite ends of the sense wire. In the CMX, the conical geometry provides a small stereo angle from which the z coordinate of track segments can be determined. Reconstructed track segments have a minimum of three hits, and a maximum of four hits in the CMU and the CMP, and 8 hits in the CMX.

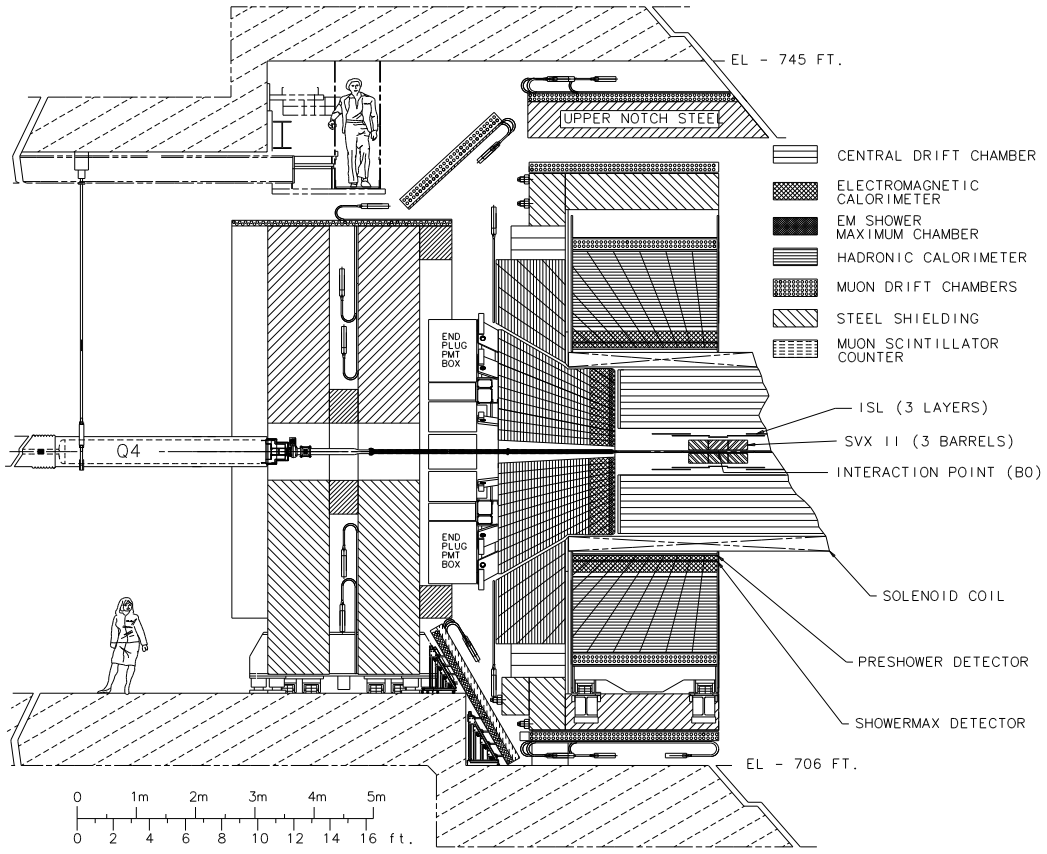

FIG. 1: Elevation view of the CDF II detector.

III. DATA SAMPLE AND EVENT SELECTION

In this section we describe the collision data and the Monte Carlo samples used in this analysis. Section III A outlines the trigger system used for the initial selection of events from the $p\bar{p}$ collisions. Section III B describes the Monte Carlo samples used for acceptance and background studies. The selection of the W+jets datasets from the triggered data samples is presented in Section III C. The $t\bar{t}$ signal is extracted from the W+jets events through the identification of candidate b hadron semileptonic decays to muons. The algorithm for identifying these decays is summarized in Section III D, and its application to the W+jets dataset is described in Section III E.

This analysis is based on an integrated luminosity of 194 ± 11 pb^{-1} [11] collected with the CDF II detector between March 2002 and August 2003 (175 pb^{-1} with the CMX detector operational).

A. $p\bar{p}$ Collision Data

CDF II employs a three-level trigger system, the first two consisting of special purpose hardware and the third consisting of a farm of commodity computers. Triggers for this analysis are based on selecting high transverse

momentum electrons and muons. The electron sample is triggered as follows: At the first trigger level events are selected by requiring a track with $P_{\rm T} > 8$ GeV/c matched to an electromagnetic calorimeter tower with $E_{\rm T} > 8$ GeV and little energy in the hadronic calorimeter behind it. At the second trigger level, calorimeter energy clusters are assembled and the track found at the first level is matched to an electromagnetic cluster with $E_{\rm T} > 16$ GeV. At the third level, offline reconstruction is performed and an electron candidate with $E_{\rm T} > 18$ GeV is required. The efficiency of the electron trigger is measured from the data and found to be $(96.2 \pm 0.6)\%$ [12]. The selection of the muon sample begins at the first trigger level with a track with $P_{\rm T} > 4$ GeV/c matched to hits in the CMU and the CMP chambers or a track with $P_{\rm T} > 8$ GeV/c matched to hits in the CMX chambers. At the second level, a track with $P_{\rm T} > 8$ GeV/c is required in the event for about 70% of the integrated luminosity, while for the remainder, triggers at the first level are fed directly to the third level. At the third trigger level, a reconstructed track with $P_{\rm T} > 18$ GeV/c is required to be matched to the muon chamber hits. The efficiency of the muon trigger, also measured directly from the data, is $(88.7 \pm 0.7)\%$ for CMU/CMP muons and $(95.4 \pm 0.4)\%$ for CMX muons [12].

B. Monte Carlo Datasets

The detector acceptance of $t\bar{t}$ events is modeled using `PYTHIA` v6.2 [13] and `HERWIG` v6.4 [14]. These are leading-order event generators with parton showering to simulate radiation and fragmentation effects. The generators are used with the CTEQ5L parton distribution functions [15]. Decays of b and c hadrons are modeled using `QQ` v9.1 [16]. Estimates of backgrounds from diboson production (WW, WZ, ZZ) are derived using the `ALPGEN` generator [17] with parton showering provided by `HERWIG`. The background from single top production (eg. $W^* \to t\bar{b}$) is simulated using `PYTHIA`. Samples of the remaining backgrounds are derived directly from the data as described in Section IV.

The detector simulation reproduces the response of the detector to particles produced in $p\bar{p}$ collisions. The same detector geometry database is used in both the simulation and the reconstruction, and tracking of particles through matter is performed with `GEANT3` [18]. The drift model for the COT uses a parametrization of a `GARFIELD` simulation [19] with parameters tuned to match COT data. The calorimeter simulation uses the `GFLASH` [20] parametrization package interfaced with `GEANT3`. The `GFLASH` parameters are tuned to test beam data for electrons and high-$P_{\rm T}$ pions and checked by comparing the calorimeter energy of isolated tracks in the collision data to their momenta as measured in the COT. Further details of the CDF II simulation can be found in [21].

C. W+Jets Dataset

From the inclusive lepton dataset produced by the electron and muon triggers described in Section III A, we select events with an isolated electron $E_{\rm T}$ (muon $P_{\rm T}$) greater than 20 GeV and $\not\!\!E_T > 20$ GeV. The isolation I of the electron or muon is defined as the calorimeter transverse energy in a cone of $\Delta R \equiv \sqrt{\Delta\eta^2 + \Delta\phi^2} < 0.4$ around the lepton (not including the lepton energy itself) divided by the $E_{\rm T}$ ($P_{\rm T}$) of the lepton. We require $I < 0.1$. The W+jets dataset is categorized according to the number of jets with $E_{\rm T} > 15$ GeV and $|\eta| < 2.0$. The decay of $t\bar{t}$ pairs gives rise to events with typically at least three such jets, while the W plus one or two jet samples provide a control dataset with little signal contamination. Jets are identified using a fixed-cone algorithm with a cone size of 0.4 and are constrained to originate from the $p\bar{p}$ collision vertex. Their energies are corrected to account for detector response variations in η, calorimeter gain instability, and multiple interactions in an event. A complete description of W+jets event selection is given in [6].

The W+jets dataset consists mainly of events of direct production of W bosons with multiple jets. This amounts also to the largest background to $t\bar{t}$ signal. As a first stage of background reduction, we define a total event energy, $H_{\rm T}$, as the scalar sum of the electron $E_{\rm T}$ or muon $P_{\rm T}$, the event $\not\!\!E_T$ and jet $E_{\rm T}$ for jets with $E_{\rm T} > 8$ GeV and $|\eta| < 2.4$. Due to the large mass of the top quark, a $t\bar{t}$ event is expected to have a large $H_{\rm T}$ compared to a W plus three or more jets event, as illustrated in Figure 2. We studied the expected amount of signal (S) and background (B) as a function of $H_{\rm T}$ using the `PYTHIA` Monte Carlo program to model the signal $H_{\rm T}$ distribution. Data is used to model the background $H_{\rm T}$ distribution. We optimized the selection of events by imposing a minimum $H_{\rm T}$ requirement which maximizes $S/\sqrt{S+B}$. We select events with $H_{\rm T} > 200$ GeV, rejecting approximately 40% of the background while retaining more than 95% of the $t\bar{t}$ signal.

There are 337 W plus three or more jet events with $H_{\rm T} > 200$ GeV in 194 pb^{-1} of data, 115 from $W \to \mu\nu$ candidates and 222 from $W \to e\nu$ candidates.

Even after the $H_{\rm T}$ cut, the expected $S{:}B$ in W plus three or more jet events is only of order 1:3. To further improve the signal to background ratio, we identify events with one or more b-jets by searching inside jets for semileptonic decays of b hadrons into muons.

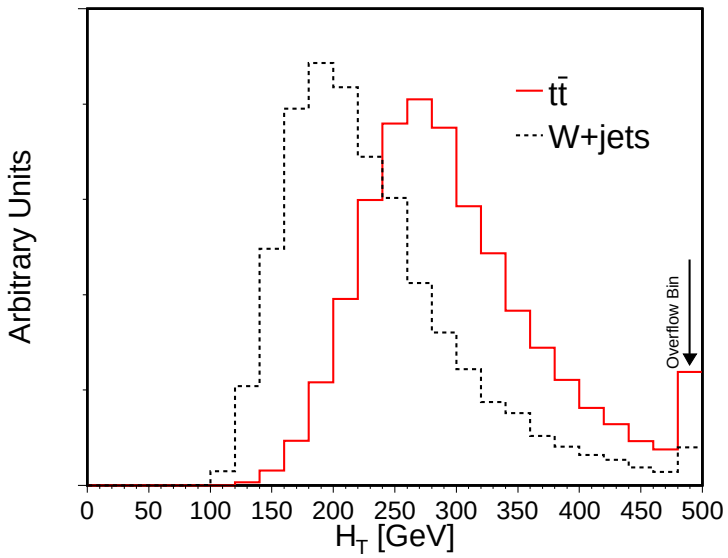

FIG. 2: $H_{\rm T}$ distributions, normalized to unity, for $t\bar{t}$ (solid line) and W+jets (dotted line) PYTHIA Monte Carlo events with three or more jets after the event selection described in the text.

D. Soft Lepton Tagging Algorithm

Muon identification at CDF proceeds by extrapolating tracks found in the central tracker, through the calorimeter to the muon chambers, and matching them to track segments reconstructed in the muon chambers. Matching is done in extrapolated position along the muon chamber drift direction (x), in the longitudinal coordinate along the chamber wires (z) when such information is available, and in the extrapolated slope compared to the slope of the reconstructed muon chamber track segment (ϕ_L). Tracks are paired with muon chamber track segments based on the best match in x for those track segments that are within 50 cm of an extrapolated COT track. In what follows we refer to the difference between the extrapolated and measured positions in x and z as dx and dz, respectively, and the extrapolated and measured slope as dϕ_L. The distributions of these variables over an ensemble of events are referred to as the matching distributions. In addition to selection based on dx and dz, the standard muon identification also requires consistency with minimum ionizing energy deposition in the calorimeters. However, in order to retain sensitivity for muons embedded in jets, the muon SLT algorithm makes full usage of the muon matching information without any requirement on the calorimeter information. The algorithm starts with high-quality reconstructed tracks in the COT, selected by requiring at least 24 axial and 24 stereo hits on the track. Some rejection for pion and kaon decays in flight is achieved by requiring that the impact parameter of the reconstructed track be less than 3 mm with respect to the beamline. The track is also required to originate within 60 cm in z of the center of the detector. Only tracks passing these cuts and extrapolating within $3\sigma(P_{\rm T})$ in x outside of the muon chambers, where $\sigma(P_{\rm T})$ is the multiple scattering width, are considered as muon candidates. Also, when a track extrapolates to greater than $3\sigma(P_{\rm T})$ in x inside the muon chambers, but no muon chamber track segment is found, the track is rejected and not allowed to be paired to other muon chamber track segments.

Candidate muons are selected with the SLT algorithm by constructing a quantity L, based on a comparison of the measured matching variables with their expectations. To construct L we first form a sum, Q, of individual χ^2 variables

$$Q = \sum_{i=1}^{n} \frac{(x_i - \mu_i)^2}{\sigma_i^2}, \tag{1}$$

where μ_i and σ_i are the expected mean and width of the distribution of matching variable x_i. The sum is taken over n selected variables, as described below. L is then constructed by normalizing Q according to

$$L = \frac{(Q - n)}{\sqrt{\mathrm{var}(Q)}}, \tag{2}$$

where the variance var(Q) is calculated using the full covariance matrix for the selected variables. The normalization is chosen to make L independent of the number of variables n; note that the distribution of L tends to a Gaussian centered at zero and with unitary width, for n sufficiently large. The correlation coefficients between each pair of variables are measured from $J/\psi \to \mu\mu$ data. The calculation proceeds by comparing the variance of the sum with the sum of the variances of each pair of χ^2 variables in Equation 1. Since the values of the matching variables are either positive or negative, according to the local coordinate system, separate correlation coefficients are used for pairs that have same-sign and opposite-sign values.

The selected variables are the full set of matching variables, x, z, ϕ_L in the CMU, CMP and CMX with the following two exceptions: The CMP chambers do not provide a measurement of the longitudinal coordinate z, and matching in ϕ_L is not included for track segments in the muon chambers that have only three hits. Because of their significantly poorer resolution, track segments reconstructed in the CMU chambers with three hits are not used. Note that a muon that traverses both the CMU and the CMP chambers yields two sets of matching measurements in x and ϕ_L and one z matching measurement, and are referred as CMUP muons. All available matching variables are used in the calculation of L for a given muon candidate. By placing an appropriate cut on L, background is preferentially rejected because hadrons have broader matching distributions than muons since the track segments in the muon chambers from hadrons are generally a result of leakage of the hadronic shower.

The widths of the matching distributions that enter into L are a combination of intrinsic resolution of the muon chambers and multiple scattering. The multiple scattering term varies inversely with P_{T} and is dominant at low P_{T}. The expected widths of the matching distributions are based on measurements of muons from J/ψ decays at low P_{T} (see Figure 3) and W and Z boson decays at high P_{T}.

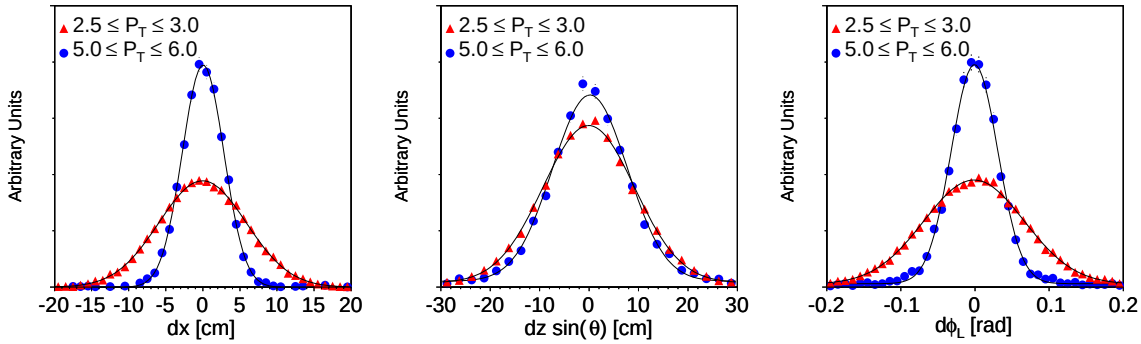

FIG. 3: Examples of muon matching distributions for the CMU in (left to right) drift direction, x, the longitudinal coordinate, z, and angle, ϕ_L. For each variable we show two P_{T} ranges, $2.5 \leq P_{\mathrm{T}} \leq 3$ GeV/c (wide distribution) and $5 \leq P_{\mathrm{T}} \leq 6$ GeV/c (narrow distribution). For the longitudinal coordinate z, we plot the product of dz by $\sin\theta$, which is the projection orthogonal to the direction of flight.

The mean values (μ_i in Equation 1) are typically zero, except for a small offset in the CMU dz. We parameterize the widths as a function of up to three variables: P_{T}, η and ϕ. These variables describe to first order the effects of multiple scattering in the detector. For the CMU detector, P_{T} is sufficient since the material traversed by a muon candidate is approximately homogenous in η and ϕ. The widths are parameterized with a second-order polynomial in $1/P_{\mathrm{T}}$ with an exponential term that describes the P_{T} range below 3 GeV/c. For the CMP detector we parameterize the widths as functions of P_{T} and ϕ to take into account the rectangular shape of the absorber outside the central calorimeter. For the CMX detector we use P_{T}, η and ϕ to account for a number of irregularities in the amount of absorber between $\eta = 0.6$ and $\eta = 1.0$. The measurement of the widths of the matching distributions as functions of P_{T}, overlayed with their fits, are shown in Figure 4.

Figure 5 (left) shows an example of the distribution of L from J/ψ decays. The number of variables used varies from two to five. Figure 5 (right) shows the efficiency of the SLT algorithm as a function of L from J/ψ data. The efficiency plateaus at about 85% for $|L| \geq 3.5$.

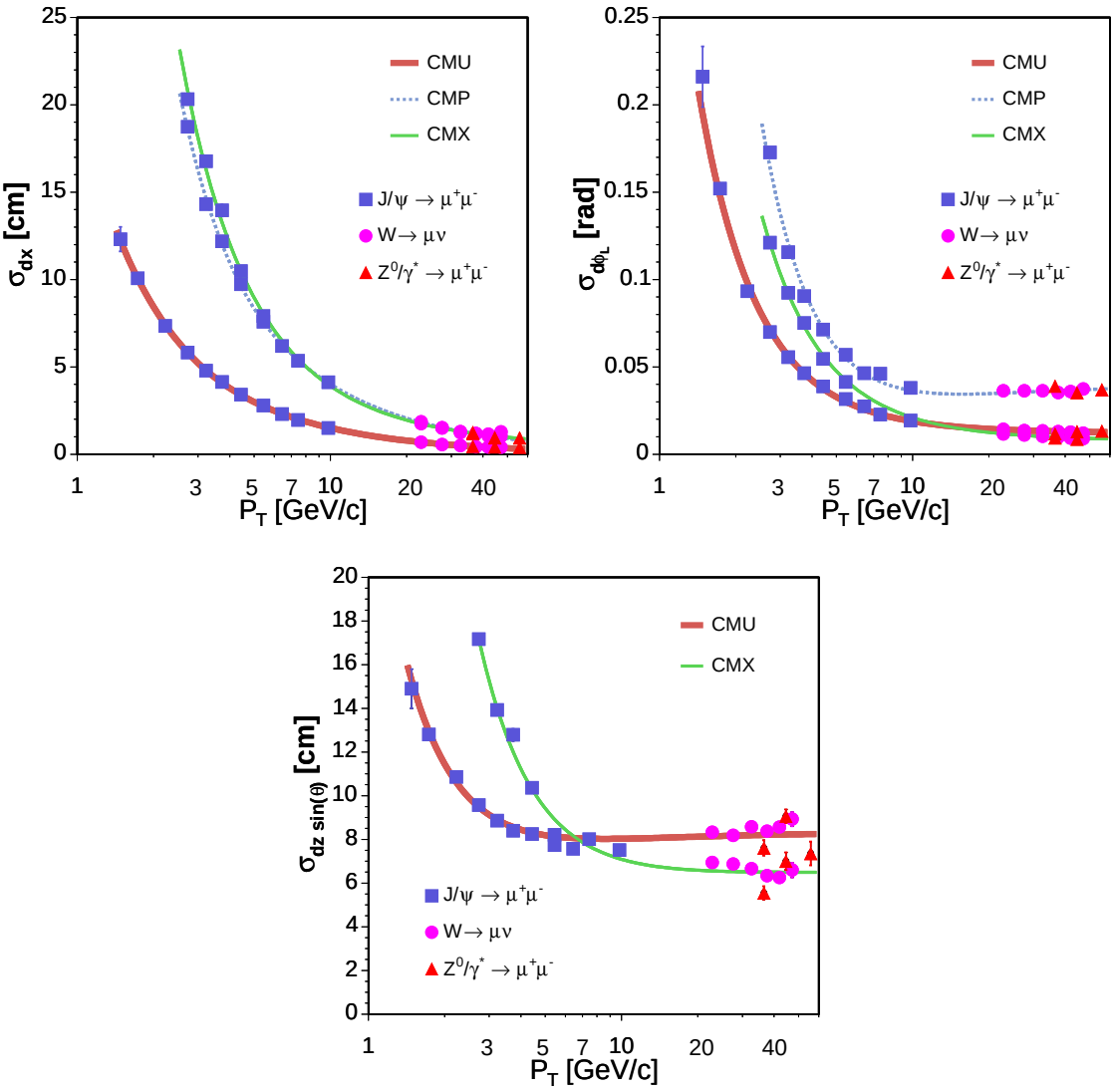

FIG. 4: Width of the matching variable distributions $(\mathrm{d}x, \mathrm{d}z, \mathrm{d}\phi_L)$ vs. P_T for each muon chambers. The data points, from J/ψ, W and Z decays, are fit to the parameterizations described in the text.

E. Event Tagging

In this analysis we seek to identify semileptonic decays of b hadrons inside jets in $t\bar{t}$ events. The transverse momentum spectrum of these muons, covering a broad range from a few GeV/c to over 40 GeV/c, is shown in Figure 6 from the `PYTHIA` Monte Carlo sample. Within the W+jets dataset defined in Section III C, we isolate a subset of events with at least one "taggable" track. A taggable track is defined as any track, distinct from the primary lepton, passing the track quality requirements described in Section III D, with $P_\mathrm{T} > 3$ GeV/c, within $\Delta R < 0.6$ of a jet axis and pointing to the muon chambers to within a 3σ multiple scattering window (the σ of the multiple scattering window is defined as the $\sigma_{\mathrm{d}x}$ shown in Figure 3). The z-coordinate of the track at the origin must be within 5 cm of the reconstructed event vertex (the vertex reconstruction is described in detail in [5]). Jets are considered "SLT tagged" if they contain a taggable track, which is also attached to a track segment in the muon chambers and the resulting muon candidate has $|L| < 3.5$.

A potentially large background arises from J/ψ decay and sequential, double semi-leptonic $b \to c \to s$ decay, resulting in one lepton from the b decay and an oppositely charged lepton from the c decay. Therefore, events are rejected if the primary lepton is of opposite charge to a SLT muon tag and the invariant mass of the pair is less than

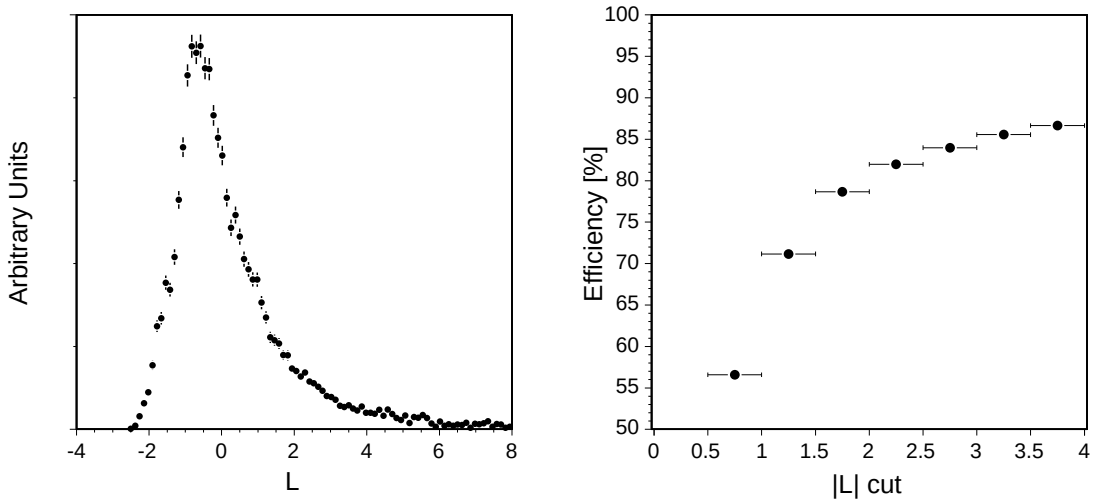

FIG. 5: Left: distribution of L from J/ψ decays. Right: the SLT efficiency as a function of the $|L|$ cut, as measured from J/ψ decay.

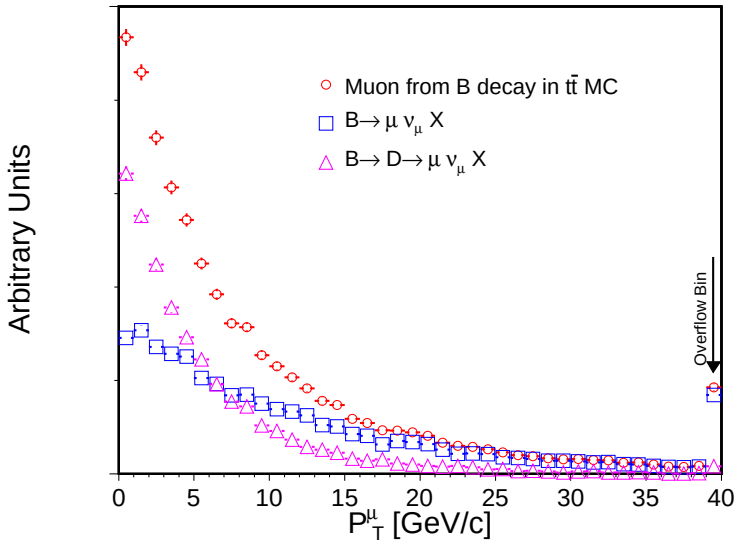

FIG. 6: $P_{\rm T}$ distribution of muons from b hadron decays in PYTHIA Monte Carlo top events. The circles are all muons from b hadron decays. The triangles are direct $B \to \mu\nu X$ decays and the squares are sequential $B \to D \to \mu\nu X$.

5 GeV/c^2. Similarly, events are also rejected if the primary lepton is a muon that together with an oppositely-charged SLT muon tag forms an invariant mass between 8 and 11 GeV/c^2 or 70 and 110 GeV/c^2, consistent with an Υ or a Z particle, respectively. The sequential decay cut and the Υ and Z removal reduce the $t\bar{t}$ acceptance by less than 1%.

Events passing all event selection cuts that have at least one taggable track are referred to as the 'pretagged' sample. There are 319 pretagged events with three or more jets, 211 in which the primary lepton is an electron and 108 in which it is a muon. Out of these events we find 20 events with a SLT tag, 15 in which the primary lepton is an electron and 5 in which it is a muon. This set of events is the $t\bar{t}$ candidate sample from which we measure the $t\bar{t}$ production cross section in Section VII.

IV. BACKGROUNDS

In this section we describe the evaluation of background events in the $t\bar{t}$ candidates sample. The background contributions are mostly evaluated directly from the data. The dominant background in this analysis is from W plus jets events where one jet produces an SLT tag. The estimate of this background relies on our ability to predict the number of such SLT tags starting from the pretagged sample. The prediction is based on the probability for a given track in a jet to yield an SLT tag, and is measured in γ+jets events. We then evaluate the systematic uncertainty on the W+jets background estimate by testing the predictive power of the measured probabilities in a variety of data samples. The W+jets background evaluation and its systematic uncertainty is described in Section IV A. After W+jets production, the next largest background is due to QCD multi-jet events. The evaluation of the QCD multi-jet contribution also relies on tagging probabilities measured in γ+jets events. However, we must account for the possible difference between the tagging probabilities for the QCD events that populate the $t\bar{t}$ candidate sample because the $\not\!\!E_T$ often comes from a mismeasured jet and not from a neutrino. The evaluation of the QCD background is described in Section IV B. An additional small source of background is due to Drell-Yan events and is estimated from the data and described in Section IV C. The remaining background contributions are relatively small and are evaluated using Monte Carlo samples, as described in Section IV D.

A. Backgrounds from W+jets

W plus jets events enter the signal sample either when one of the jets is a b-jet or a c-jet with a semileptonic decay to a muon, or a light quark jet is misidentified as containing a semileptonic decay ("mistagged"). We refer to these background events as W+heavy flavor and W+"fakes", respectively. W+heavy flavor events include $Wb\bar{b}$, $Wc\bar{c}$ and Wc production. We measure their contribution by constructing a "tag matrix" that parameterizes the probability that a taggable track with a given $P_{\rm T}$, η and ϕ, in a jet with $E_{\rm T} > 15$ GeV, will satisfy the SLT tagging requirement described in Section III E. The variables η and ϕ are measured at the outer radius of the COT with respect to the origin of the CDF II coordinate system. The tag matrix is constructed using jets in γ+jets events with one or more jets. The tag probability is approximately 0.7% per taggable track, and includes tags from both fakes and heavy flavor. The tag rate as a function of each of the matrix parameters (integrated over the remaining two) is shown in Figure 7. The features in the tag rate vs. η and ϕ plots are a result of calorimeter gaps and changes in the thickness of the absorber before the muon chambers. The matrix is binned to take account of these variations. The bottom right plot shows the tag rate as the function of the $|L|$ cut for each muon category. The tag rate is higher for the CMP-only muons due to the smaller amount of absorber material that results from cracks in the calorimeter where there is no coverage by the CMU chambers.

We apply the tag matrix to all pretagged events in the signal region according to:

$$N^{\rm tag}_{\rm predicted} = \sum_{\rm events} \left[\sum_{i=1}^{N_{\rm trk}} \sum_{j=i+1}^{N_{\rm trk}} (\mathcal{P}_i + \mathcal{P}_j - \mathcal{P}_i \cdot \mathcal{P}_j) \right], \tag{3}$$

where the first sum runs over each event in the pretagged sample, and the subsequent sums are over each taggable track in the event. $\mathcal{P}_i$ is the probability from the tag matrix for tagging the i-track with parameters P_{T_i}, η_i and ϕ_i. Note that the sum over the events in Equation 3 includes any $t\bar{t}$ events that are in the pretagged sample. We correct for the resulting overestimate of the background at the final stage of the cross section calculation, since the correction depends on the measured tagging efficiency (see Section VII).

A fraction, F_{QCD}, of the events in the signal region are QCD events (such as $b\bar{b}$ or events in which a jet fakes an isolated lepton, see Section IV B) for which the background is estimated separately. Therefore, we explicitly exclude their contribution to $N^{\rm tag}_{\rm predicted}$ and obtain the predicted number of tagged W+jets background events

$$N^{Wj-{\rm tag}}_{\rm predicted} = (1 - F_{QCD}) \cdot N^{\rm tag}_{\rm predicted}. \tag{4}$$

The estimated W+fakes and W+heavy flavor background is given in the third line of Table VI.

The above technique relies on the assumption that the tagging rate in jets of the γ+jets sample is a good model for the tagging rate of the jets in W+jets events. The assumption is plausible because the SLT tagging rate in generic jet events is largely due to fakes. We have studied the heavy flavor content of the tags in the γ+jets sample using the overlap sample between SLT tags and displaced vertex tags identified with the silicon tracker [5]. We find that (21.0±1.4)% of the tags in the γ+jets sample are from heavy flavor. We have used `MADEVENT` [22] to do generator-level

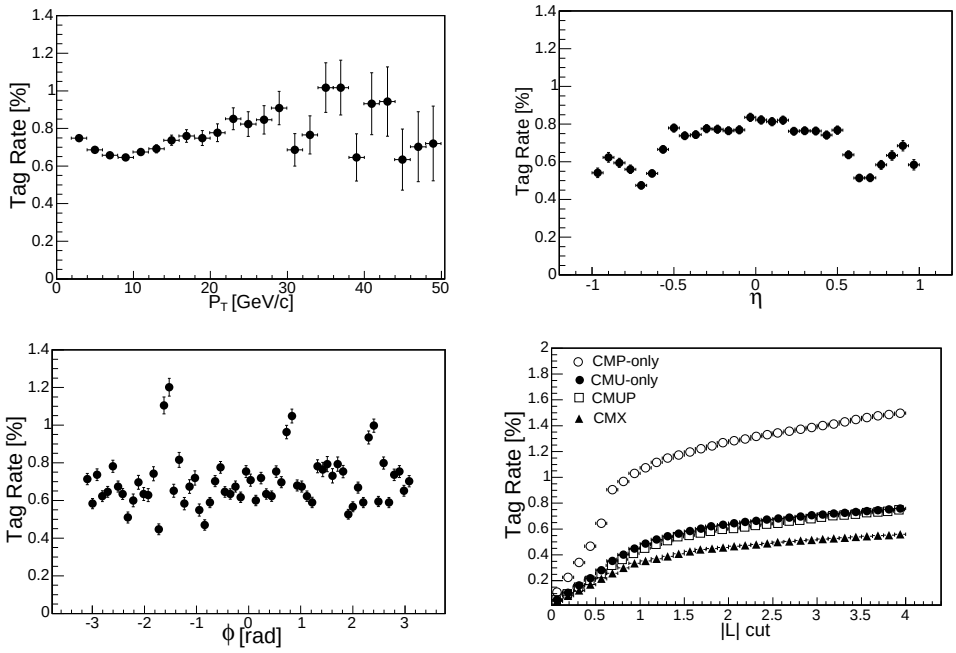

FIG. 7: Tag rates in the photon plus jets sample as a function of each of the tag-rate matrix parameters. Each plot is integrated over the two parameters not shown. The bottom right plot shows the tag rate as the function of the $|L|$ cut for each of the muon categories.

comparisons of the heavy-flavor fractions of W+jets events with those from the γ plus jets events that make up the tag matrix. We find that the γ+jets sample used to make the tag matrix has approximately 30% more heavy flavor than the $W+ \geq 3$ jet events. Since SLT tags in γ+jets events are dominantly fakes, this difference affects the background prediction in W+jets events at only the few-percent level.

Given the limitations of a generator-level, matrix element Monte Carlo study of the heavy flavor content of the γ+jets and W+jets samples, we do not use the `MADEVENT` study to evaluate the systematic uncertainty on the background due to tagged W+jets events. Instead we test the accuracy of the tag matrix for predicting SLT muon tags by using it to predict the number of tags in a variety of samples with different heavy flavor content. We check Z plus jets events, events triggered on a jet with $E_{\rm T}$ thresholds of 20, 50, 70 and 100 GeV (called Jet 20, Jet 50, Jet 70 and Jet 100), or triggered on four jets and the scalar sum of transverse energy in the detector (called SumET). We find that the matrix predicts the observed number of tags in each of these samples to within 10%, as shown in Figure 8, and we use this as the systematic uncertainty on the prediction from the tag matrix.

B. QCD Background

We refer to events with two or more jets in which the decay of a heavy-flavor hadron produces a high-$P_{\rm T}$ isolated lepton, or in which a jet fakes such a lepton, as QCD events. These events enter the sample when, in addition to the high-$P_{\rm T}$ isolated lepton, a muon from a heavy flavor decay gives an SLT tag, or there is a fake tag. We measure this background directly from the data.

To estimate the QCD component we first use the distribution of pretagged events in the plane of $\not\!\!E_T$ vs. isolation, I, of the primary lepton. We populate this plane with lepton plus jets events according to the event $\not\!\!E_T$ and I. We consider four regions in the plane:

$$A : \not\!\!E_T < 15 \;\; I > 0.2$$
$$B : \not\!\!E_T < 15 \;\; I < 0.1$$
$$C : \not\!\!E_T > 20 \;\; I > 0.2$$
$$D : \not\!\!E_T > 20 \;\; I < 0.1$$

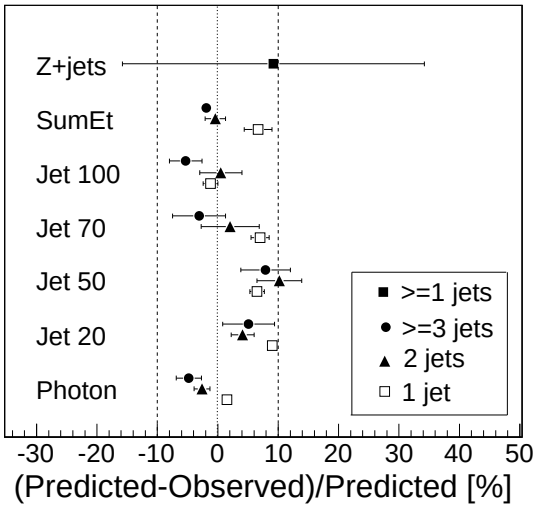

FIG. 8: The percent difference between the number of predicted and measured tags in a variety of samples for different jet multiplicities, as marked. Jet multiplicities do not include the trigger object (photon or jet). The three photon points contain the events that make up the tag matrix. Their average is zero by definition and is show by the line centered at zero. The dashed lines at ±10% indicate the systematic uncertainty.

where Region D is the $t\bar{t}$ signal region. The distribution of events, with one or more jets, in the $\not\!\!E_T$ vs. I regions is shown in Figure 9.

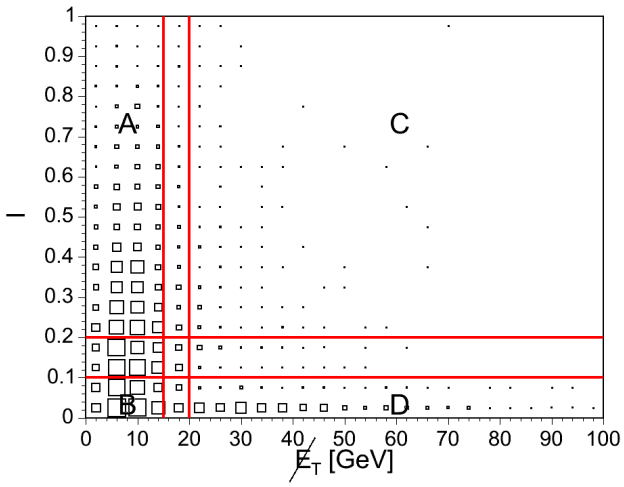

FIG. 9: Distribution of events with ≥1 jet in $\not\!\!E_T$ vs. I. Regions A,B,C are defined in the text and are used to calculate the fraction of QCD events in region D (the signal region) according to Equation 5.

In order to populate Regions A, B and C with only QCD events, we correct the number of events for the expected contamination of W+jets and $t\bar{t}$ events in those regions using expectations from Monte Carlo simulations. The corrections range from a few percent in electron plus one-jet events, to (57±34)% in Region B in muon plus three or more jet events.

Assuming that the variables $\not\!\!E_T$ and I are uncorrelated for the QCD background, we calculate the fraction of QCD events in Region D, F_{QCD}, as:

$$F_{QCD} = \left.\frac{N_D^{QCD}}{N_D}\right|_{\text{pretagged}} = \left.\frac{N_B \cdot N_C}{N_A \cdot N_D}\right|_{\text{pretagged}}, \tag{5}$$

where N_D^{QCD} is the total number of pretagged QCD events in the signal region, and N_i represent the number of events in region i. The measured fractions are shown in Table I.

To estimate the number of tagged QCD events in the signal region, we multiply F_{QCD} by the tagging probability for QCD events. However, this tagging probability is not necessarily given by the tag matrix probabilities which are designed for jets in W+jets events. Mismeasurement in the jet energies and differences in kinematics between W+jets and QCD events may affect the tagging probabilities. W+jets events have $\not\!\!E_T$ from the undetected neutrino, whereas QCD events have $\not\!\!E_T$ primarily from jet mismeasurement. Jet mismeasurement is correlated with fake tags due to energy leakage from the calorimeter through calorimeter gaps or incomplete absorption of the hadronic shower, both of which can result in track segments in the muon chambers. W+jets events have a primary lepton from the W decay, whereas QCD events have a primary lepton that is either a fake or a result of a semileptonic decay of heavy flavor. The presence of a lepton from heavy flavor decay typically enhances the tag rate. Figure 10 shows the ratio of the number of measured tags in the Jet 20 sample to the number of tags predicted by the tag matrix as a function of $\not\!\!E_T$. As expected, in QCD events with large $\not\!\!E_T$ we find a tag rate significantly larger than that described by the tag matrix.

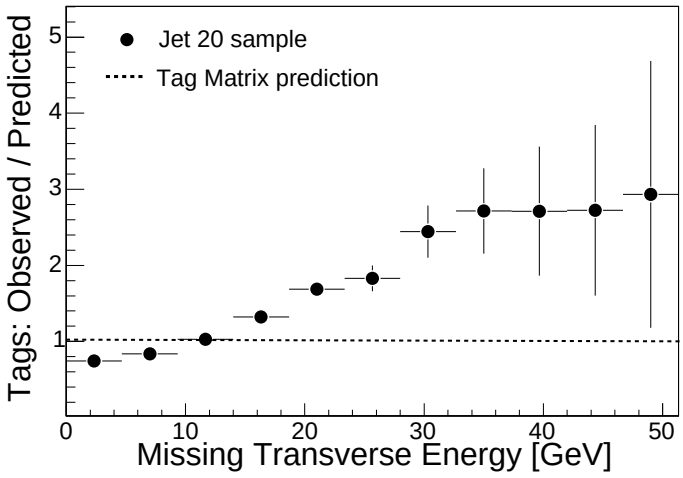

FIG. 10: The ratio of the number of observed tags to tags predicted using the tag matrix, as a function of $\not\!\!E_T$, in events with at least one jet with measured energy above 20 GeV.

We find that the prediction of the tag matrix can be renormalized to properly account for the tag rates in QCD events with a single multiplicative factor, which we call k. We measure k using events in region C by comparing the number of SLT tags found to the number predicted by the tag matrix. Since the signal region contains only isolated ($I < 0.1$) primary leptons, we reject events in the measurement of k in which the SLT tag is within $\Delta R < 0.5$ of the primary lepton. After this requirement we do not find any dependence of k on the isolation of the primary lepton. Figure 11 shows the ratio of measured to predicted tags in events in region C as a function of $H_{\rm T}$. The tag rate above $H_{\rm T} = 200$ GeV is approximately flat and is not much different from the prediction of the tag matrix (dashed line in Figure 11). However, QCD events at lower $H_{\rm T}$ have a significantly different tag rate than that predicted by the tag matrix. As shown in Figure 12, F_{QCD} also has an $H_{\rm T}$ dependence for events with 1 or 2 jets, but is flat within the statistical uncertainty for three or more jets.

The number of QCD background events is calculated as:

$$N_{QCD} = \langle F_{QCD} \cdot k \rangle \cdot N^{\rm tag}_{\rm predicted}, \tag{6}$$

where $N^{\rm tag}_{\rm predicted}$ is given in Equation 3 and the brackets represent the product of F_{QCD} and k convoluted with the $H_{\rm T}$ distribution of QCD events from region C. In the control region (1 and 2 jets), the fits of F_{QCD} vs. $H_{\rm T}$, shown

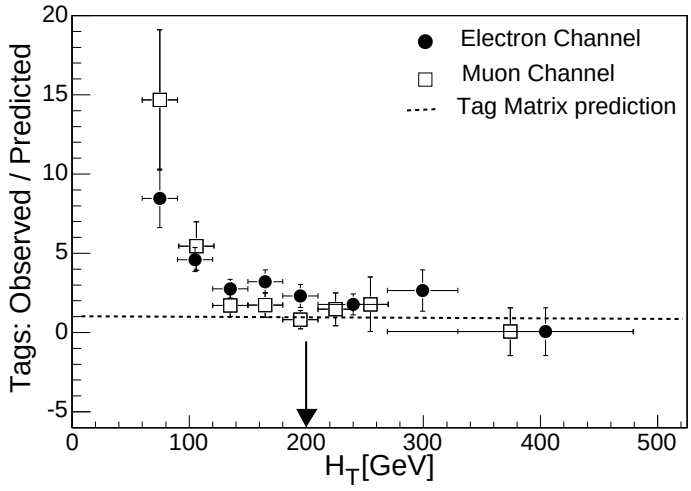

FIG. 11: The ratio of the observed rate of tags to that predicted, as a function of $H_{\rm T}$ in region C for events with one or more jets. The arrow at 200 GeV shows where the selection cut for the $t\bar{t}$ signal sample is placed.

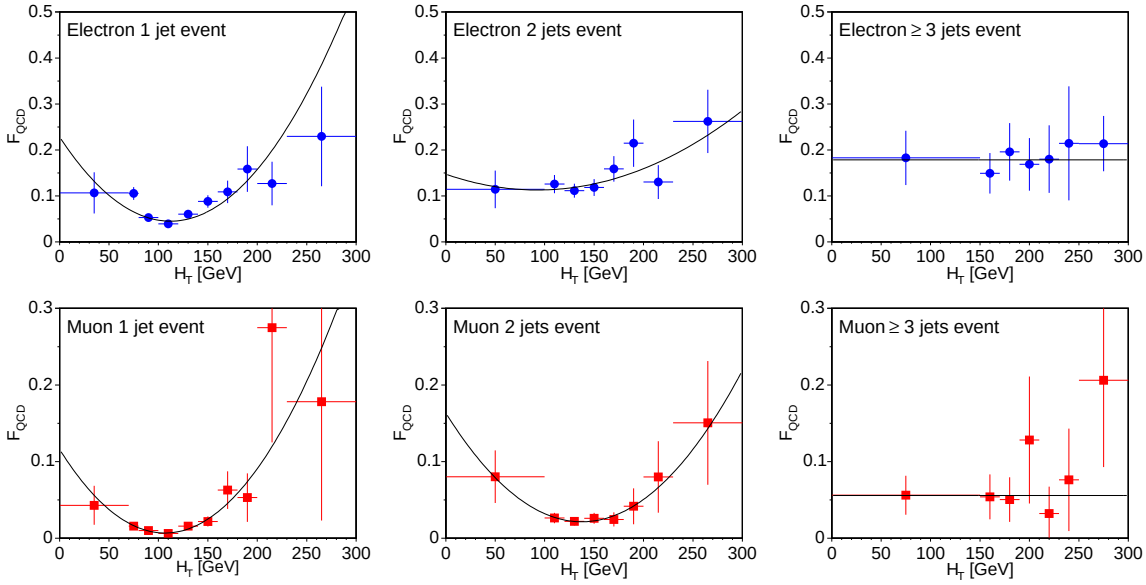

FIG. 12: F_{QCD} measured according to Equation 5 as a function of $H_{\rm T}$ in electron events (top) and muon events (bottom) with (left to right) 1, 2 or $\geq$ 3 jets.

in Figure 12, are convoluted with k vs. $H_{\rm T}$, shown in Figure 11. For events with three or more jets, since there is no visible $H_{\rm T}$ dependence for either F_{QCD} or k, we simply multiply their average values for $H_{\rm T} > 200$ GeV. Measured values of k times F_{QCD} are given in Table I. The procedure by which F_{QCD} is determined as a function of $H_{\rm T}$ is important because the ratios between the four different regions of the $\not\!\!E_T$ and I kinematic plane, calculated in separate ranges of $H_{\rm T}$ and then averaged, does not necessarily correspond to the same ratios taken while integrating over the full $H_{\rm T}$ range. The uncertainties on the 1 and 2 jet events are conservatively taken as the difference between the central value and the result of the straight product of F_{QCD} and k. The straight product corresponds to ignoring the $H_{\rm T}$ dependence as well as any other variable's dependence of F_{QCD} and k.

TABLE I: QCD fraction, given by Equation 5, and the $H_{\rm T}$-averaged product of k and the QCD fraction.

Jet multiplicity	1 jet	2 jet	3 jets	≥ 4 jets	≥ 3 jets
			Muons		
F_{QCD}	0.03 ± 0.002	0.039 ± 0.004	0.023 ± 0.011	0.146 ± 0.088	0.044 ± 0.016
$\langle k_\mu \cdot F_{QCD} \rangle$	0.02 ± 0.07	0.05 ± 0.51	0.01 ± 0.01	0.09 ± 0.07	0.03 ± 0.02
			Electrons		
F_{QCD}	0.145 ± 0.007	0.177 ± 0.010	0.135 ± 0.032	0.163 ± 0.051	0.145 ± 0.028
$\langle k_e \cdot F_{QCD} \rangle$	0.24 ± 0.31	0.41 ± 0.12	0.16 ± 0.046	0.20 ± 0.07	0.17 ± 0.04

C. Drell-Yan Background

Drell-Yan events can enter the sample when they are produced with jets and one muon is identified as the primary muon while the second muon is close enough to a jet to be tagged. Residual Drell-Yan background that is not removed by the dimuon and sequential decay rejection described in Section III E, is estimated from the data. We use events inside the Z-mass window ($76 - 106$ GeV/c^2), which are otherwise removed from the analysis by the Z-mass cut, to measure the number of events that would pass all our selection requirements including the SLT tag, $N_{\rm inside}^{\rm tags}$. Because of the limited sample size of Z+jets events, we use $Z + 0$ jet events without the $\not\!\!E_T$ and $H_{\rm T}$ requirements to find the ratio of events outside the Z-mass window to those inside the window, $R_{Z/\gamma^*}^{\rm out/in}$, and a first-order estimate of the number of expected Drell-Yan events outside of the Z-mass window is calculated as:

$$N_{DY} = N_{\rm inside}^{\rm tags} \cdot R_{Z/\gamma^*}^{\rm out/in}. \tag{7}$$

This estimate assumes that $R_{Z/\gamma^*}^{\rm out/in}$ does not depend on the number of jets in the event. We assign a systematic uncertainty of 33% for this assumption based on the largest deviation between $R_{Z/\gamma^*}^{\rm out/in}$ for ALPGEN Z/γ^* plus zero jet events compared with 1, 2 or $\geq$3 jets events.

The first-order estimate is then corrected by the relative efficiency inside and outside the Z-mass window of the $\not\!\!E_T$, $H_{\rm T}$, and SLT-jet requirements, which we measure using Z/γ^*+jets Monte Carlo events. The Drell-Yan background estimates are listed in the sixth line of Table VI.

D. Other Backgrounds

Remaining background sources are due to WW, WZ, ZZ, $Z \to \tau\tau$ and single top production. Diboson events can enter the sample when there are two leptons from a Z and/or a W decay and jets. One lepton passes the primary lepton requirements while the second is available to pass the SLT requirement if it is close to a jet. The $\not\!\!E_T$ in these events can either come from a W-boson decay or from an undetected lepton in a Z-boson decay. $Z \to \tau\tau$ events can enter the sample when the Z is produced in association with jets and one τ decays to a high-$P_{\rm T}$ isolated electron or muon, while the second τ produces an SLT muon in its decay. Electroweak single top production gives rise to an event signature nearly identical to $t\bar{t}$ when there are additional jets from gluon radiation.

TABLE II: Summary of the expected number of background events for those sources derived from Monte Carlo simulations, and the cross sections used in Equation 8. The quoted uncertainties come from Monte Carlo samples size and the uncertainty on the theoretical cross sections.

	1 jet	2 jets	3 jets	≥ 4 jets	≥ 3 jets
WW [23]	0.64±0.15	0.99±0.18	0.12±0.07	0.029±0.033	0.15±0.08
WZ [23]	0.11±0.07	0.22±0.09	0.03±0.04	0.003±0.006	0.03±0.04
ZZ [23]	0.013±0.010	0.025±0.015	0.007±0.007	0.004±0.004	0.010±0.010
$Z \to \tau^+\tau^-$ [24]	0.34±0.16	0.10±0.05	0.006±0.003	0.002±0.001	0.008±0.004
Single top [25]	0.50 ± 0.03	0.94 ± 0.06	0.15 ± 0.01	0.035 ± 0.003	0.19 ± 0.01

None of the above background sources are completely accounted for by the application of the tag matrix to the pretagged event sample because these backgrounds have a significant source of muons from, for instance, W and Z decay. Therefore, we independently estimate their contributions to the background using Monte Carlo samples

normalized to the cross sections referenced in Table II. In modeling the SLT tagging of such events in the Monte Carlo samples, we explicitly exclude the mistag contribution which is taken in to account in the application of the tag matrix to the pretagged sample. The background for each source is estimated as:

$$N_i = \sigma_i \cdot A_i \cdot \epsilon_{\mathrm{tag},i} \cdot \int \mathcal{L}\mathrm{dt}, \tag{8}$$

where σ_i is the theoretical cross section for the particular background source, A_i is the acceptance for passing the pretagged event selection, $\epsilon_{\mathrm{tag},i}$ is the SLT tagging efficiency and $\int \mathcal{L}\mathrm{dt}$ is the integrated luminosity of the overall data sample. The expected background contributions are shown, as a function of jet multiplicity, in Table II.

V. TOTAL $t\bar{t}$ ACCEPTANCE

We factorize the efficiency for identifying $t\bar{t}$ events into the geometric times kinematic acceptance and the SLT tagging efficiency. The acceptance includes all the cuts described in Sections III C as well as the invariant mass cut described in Section III E, and is evaluated assuming a top mass of 175 GeV/c^2. The tagging efficiency is the efficiency for SLT-tagging at least one jet in events that pass the geometric and kinematic selection. We describe each piece below.

A. Geometric and Kinematic Acceptance

The acceptance is measured in a combination of data and Monte Carlo simulations. Simulations are done using the PYTHIA Monte Carlo program [13]. The primary lepton identification efficiency is measured in Z-boson decays acquired with a trigger that requires a single high-P_{T} electron or muon. The efficiency is measured using the lepton from the Z-boson decay that is unbiased by the trigger, and the identification efficiency in the Monte Carlo sample is scaled to that measured in the data [6]. The acceptance, as a function of the number of identified jets above 15 GeV, is shown in Table III. These numbers include the measured efficiencies of the high-P_{T} lepton triggers.

TABLE III: Acceptance for $t\bar{t}$ events as a function of jet multiplicity from PYTHIA Monte Carlo sample, corrected for the data/MC ratio for tight lepton ID efficiencies and the primary lepton trigger efficiency. The uncertainties listed are statistical only.

	W+ 1 jet	W + 2 jets	W + 3 jets	W + $\geq$ 4 jets	W + $\geq$ 3 jets
$W \to e\nu$ (%)	0.204±0.005	1.05±0.01	1.79±0.02	2.27±0.02	4.06±0.02
$W \to \mu\nu$ (CMUP) (%)	0.095±0.003	0.501±0.007	0.861±0.007	1.12±0.01	1.98±0.01
$W \to \mu\nu$ (CMX) (%)	0.045±0.002	0.235±0.006	0.388±0.007	0.507±0.008	0.90±0.01

B. SLT Efficiency

The efficiency for the reconstruction of the COT track is taken directly from Monte Carlo simulation. The reconstruction efficiencies of muon chamber track segments are also taken from the simulation and scaled to the values measured in the data using the lepton in Z-boson decays unbiased by the trigger. The muon identification efficiency of the SLT algorithm is measured in data using J/ψ and Z decays. We use events acquired with triggers that demand a single muon, and use only the muon not biased by the trigger. The efficiency is defined as the ratio of muons that satisfy the SLT tagging requirement over the number of taggable tracks attached to track segments in the muon chambers. In the calculation of the efficiency a background linear in invariant mass is subtracted from the J/ψ and Z peaks. The measured efficiency vs. P_{T} is shown in Figure 13 for muons with $|\eta| < 0.6$ (CMU and/or CMP) and for muons with $0.6 \leq |\eta| \leq 1.0$ (CMX). The decrease in efficiency with increasing P_{T} is a result of non-Gaussian tails in the components of L.

Since the efficiency measurement is dominated by isolated muons, whereas the muons in b-jets tend to be surrounded by other tracks, we have studied the dependence of the efficiency on the number of tracks, N_{trk}, above 1 GeV/c in a cone of $\Delta R = 0.4$ around the muon track. We find no significant efficiency loss, although the precision of the measurement is poor near $N_{\mathrm{trk}} = 6$, the mean expected in $t\bar{t}$ events. We include a systematic uncertainty to account

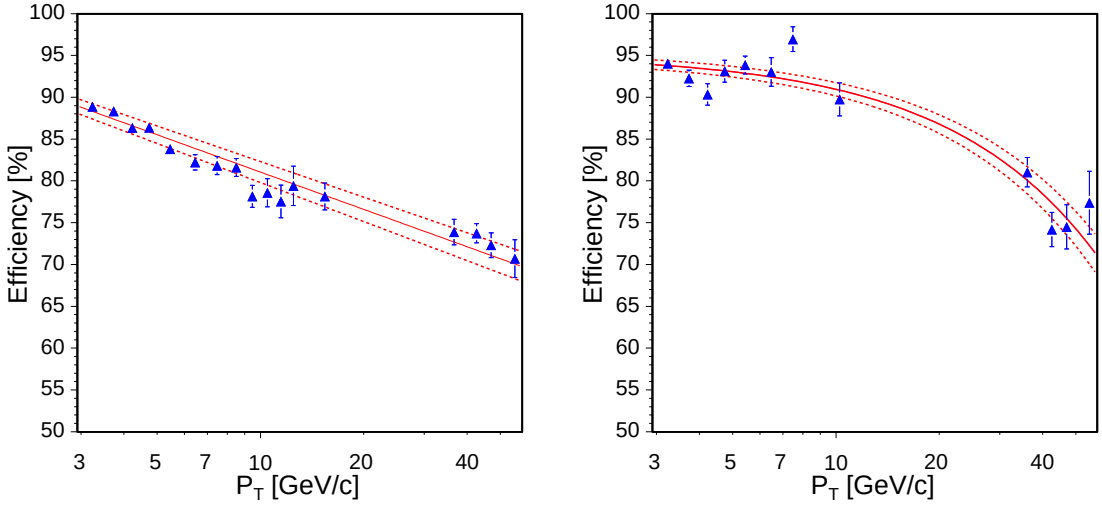

FIG. 13: The SLT efficiency for $|\eta| < 0.6$ (left) and $|\eta| \geq 0.6$ (right) as a function of P_T, measured from J/ψ and Z data for $|L| < 3.5$. The dotted lines are the $\pm 1\sigma$ statistical uncertainty on the fit which is used in the evaluation of the systematic uncertainty.

for this by fitting the efficiency vs. $N_{\rm trk}$ to a linear function and evaluating this function at the mean $N_{\rm trk}$ expected in $t\bar{t}$ events. The systematic uncertainty on the efficiency for at least one SLT tag in a $t\bar{t}$ event from this effect is $+0\%$, -8%.

The detector simulation does not properly reproduce the non-Gaussian tails of the muon matching distributions. Therefore the measured efficiencies, shown in Figure 13, are applied directly to a generated muon in the Monte Carlo sample when evaluating the efficiency for tagging a $t\bar{t}$ event. This accounts for tagging of semileptonic heavy flavor decays in $t\bar{t}$ events (including charm decays from $W \to c\bar{s}$). Events from $t\bar{t}$ can also be mistagged when a tag results from a fake muon or a decay-in-flight. We account for this effect in the tagging efficiency evaluation by allowing events that are not tagged by muons from heavy flavor decays to be tagged by other charged tracks using the tagging probabilities from the tag matrix, as described in Section IV. Since the heavy flavor component of the tagging efficiency has already been accounted for, the generic-track tagging probabilities are corrected downwards for the measured 21% heavy flavor component of the tag matrix (Section IV A). The overall efficiency for finding one or more SLT tags in a $t\bar{t}$ event ("tagging efficiency") is shown in Table IV. Mistags account for approximately 25% of the $t\bar{t}$ tagging efficiency. Because a small portion of the integrated luminosity was accumulated before the CMX was fully functional, we break the efficiency into pieces with and without the CMX. This is taken into account in the final cross section denominator. The total $t\bar{t}$ detection efficiency is the product of the acceptance and the tagging efficiency.

As noted above, the SLT efficiency has been parameterized using muons that tend to be isolated from other activity. To further check that this efficiency measurement is representative of muons in or near jets, we use a high-purity $b\bar{b}$ sample, derived from events triggered on 8 GeV electrons or muons. These events are enriched in semileptonic b-hadron decays. To select this sample, we require that the events have two jets above 15 GeV. One jet must be within $\Delta R = 0.4$ of the primary electron or muon (the "lepton jet"). For jets associated with muons, the energy is corrected to account for the muon $P_{\rm T}$. The second jet (the "away jet") in the event is chosen as the jet above 15 GeV with maximum separation in azimuth ($\geq$2 radians) from the lepton jet. Both jets are required to have a secondary vertex reconstructed and tagged by the SecVtx algorithm [5] ("SecVtx-tagged"). This results in a $b\bar{b}$ sample with a purity of approximately 95% [26]. We measure the SLT acceptance times efficiency for semileptonic decays to muons in the away jet in a `HERWIG` dijet Monte Carlo sample. Monte Carlo events are subject to the same event selection, as described above, used for the $b\bar{b}$ data sample. The efficiency parametrization measured from the data is applied in the same way as in the $t\bar{t}$ Monte Carlo sample. The derived efficiency times acceptance per b-jet is applied to the data to predict the number of SLT tags in the away jet. There are 7726 SecVtx-tagged away jets in which the lepton jet is from a muon and 2233 in which it is from an electron. In these events we predict 388 ± 54 tags in the away jet opposite a muon jet and 116 ± 17 tags in the away-jet opposite an electron jet. We find 353 and 106 respectively. We conclude that the efficiency for SLT-tagging muons from semileptonic decays of heavy flavor in jets is well modeled by our simulation.

TABLE IV: $t\bar{t}$ event tagging efficiency for SLT muons as a function of jet multiplicity from PYTHIA Monte Carlo sample. Uncertainties are statistical only.

	W + 1 jet	W + 2 jets	W + 3 jets	W + $\geq$ 4 jets	W + $\geq$ 3jets
$W \to e\nu$ w/CMX (%)	9.5 ± 0.8	13.1 ± 0.4	14.7 ± 0.3	15.9 ± 0.3	15.4 ± 0.2
$W \to e\nu$ w/o CMX (%)	6.7 ± 0.7	10.3 ± 0.4	11.5 ± 0.3	12.4 ± 0.3	12.0 ± 0.2
$W \to \mu\nu$ w/CMX (%)	7.2 ± 0.8	12.3 ± 0.5	13.3 ± 0.3	16.1 ± 0.3	14.9 ± 0.2
$W \to \mu\nu$ w/o CMX (%)	5.0 ± 0.8	9.6 ± 0.5	10.3 ± 0.4	12.8 ± 0.3	11.7 ± 0.3

VI. SYSTEMATIC UNCERTAINTIES

Systematic uncertainties in this analysis come from uncertainties in the Monte Carlo modeling of the acceptance, knowledge of the SLT tagging efficiency, the effect on the acceptance of the uncertainty on the jet energy calibration, uncertainties on the background predictions, and the uncertainty on the luminosity.

Uncertainties in the Monte Carlo modeling of acceptance include effects of parton distribution functions (PDFs), initial-state radiation (ISR), final-state radiation (FSR), and the calibration of the measured jet energy. These are estimated by comparing different choices for PDFs, varying ISR, FSR and the jet energy in the Monte Carlo programs and comparing the results from the PYTHIA generator with those from HERWIG. A complete description of the evaluation of these uncertainties appears in [6]. The total systematic uncertainty on the acceptance due to these factors is $\pm 6.1\%$. Possible variations of the lepton ID efficiency in events with multiple jets are an additional source of systematic uncertainty on the acceptance. We use a data to Monte Carlo scale factor for the lepton ID efficiency that is taken from $Z \to ee$ and $Z \to \mu\mu$ data and Monte Carlo samples. These samples contain predominantly events with no jets. A 5% systematic uncertainty on the scale factor is estimated by convoluting the scale factor itself, measured as a function of ΔR between the lepton and the nearest jet, with the ΔR distribution of leptons in $\geq$3 jet $t\bar{t}$ events [6]. Adding the uncertainties in quadrature gives a total Monte Carlo modeling systematic uncertainty on the acceptance of $\pm 8.0\%$.

There are several factors that contribute to the systematic uncertainty on the SLT tagging efficiency. The uncertainty due to our knowledge of the $P_{\rm T}$ dependence is determined by varying the efficiency curves used in the $t\bar{t}$ Monte Carlo sample according to the upper and lower bands in Figures 13. We find that the tagging efficiency for $t\bar{t}$ changes by $\pm 1\%$ from its central value. An additional source of systematic uncertainty for the tagging efficiency comes from the fact that we implicitly use the Monte Carlo tracking efficiency for taggable tracks. As these tracks can be in dense environments in or near jets, we expect the efficiency to be somewhat less than for isolated tracks. Studies done by embedding Monte Carlo tracks in jets in both data and Monte Carlo events indicate that the Monte Carlo tracking efficiency in dense environments is a few percent higher than in data. We assign a $\pm 5\%$ systematic uncertainty to the tagging efficiency for this effect. As described in Section V B the systematic uncertainty due to the modeling of the isolation dependence of the tagging efficiency is $+0\%$, -8%. Finally, the statistical uncertainty on the measurement of the SLT tagging efficiency in $t\bar{t}$ events, differences between PYTHIA and HERWIG, the uncertainty on the semileptonic branching fraction for B mesons and the estimation of the heavy flavor content of the mistag matrix also contribute to the systematic uncertainties. Adding these contributions in quadrature gives an overall systematic uncertainty for the tagging efficiency of $+8\%$, -11%. Note that the uncertainty on the tagging efficiency affects also the backgrounds determination. The reason is that $t\bar{t}$ events need to be subtracted from the pretagged sample which is used in Equation 3 to determine the W+jets background. We take this effect into account when calculating the uncertainty on the cross section.

Uncertainties on the tag matrix are determined by the level of agreement between observed tags and predictions in a variety of samples, as described in Section IV. The uncertainty on the W+fakes and $Wb\bar{b} + Wc\bar{c} + Wc$ prediction is $\pm 10\%$.

To determine the uncertainties on the QCD background prediction in events with three or more jets, we define a control sample from the $\not\!\!E_T$ vs. lepton isolation plane, where the primary lepton isolation parameter I is between 0.1 and 0.2 and the event has $\not\!\!E_T > 20$ GeV. After subtracting expected contributions from W and $t\bar{t}$ events, all events in this region are expected to be QCD. We determine the systematic uncertainty on the QCD background prediction by comparison of the observed and predicted number of events in this control region. A 50% systematic uncertainty is assigned to the F_{QCD} measurement for muons and 20% for electrons. We combine this with the statistical uncertainty on F_{QCD}, the uncertainty on the correction factor k, both given in Table I and the 10% systematic uncertainty due to the application of the tag matrix. The total QCD background uncertainty is $\pm 67\%$ and $\pm 19\%$ for muons and electrons, respectively. These values are determined taking into account the correlation between the estimate of the

QCD background and the estimate of the W+fakes and W+heavy flavor backgrounds (Equations 4 and 6). We add in quadrature the separate effects on the cross section of the QCD uncertainties for electrons and muons.

The systematic uncertainty on the small Drell-Yan background is dominated by its statistical uncertainty. We also include a 33% relative uncertainty to account for changes in the shape of the Drell-Yan spectrum with the number of jets in the event, as described in Section IV C. Uncertainties on the Monte Carlo background predictions come from uncertainties in the cross sections for the various processes and from the event sizes of the Monte Carlo samples.

The systematic uncertainties and the corresponding shift of the measured cross section value are summarized in Table V.

TABLE V: Summary of systematic uncertainties. The shift $\Delta\sigma_{t\bar{t}}$ of the measured cross section value assumes the cross section calculated in Section VII.

Source	Fractional Sys. Uncert. (%)	$\Delta\sigma_{t\bar{t}}$ (pb)
Acceptance Modeling	± 8	$\left\{ \begin{array}{l} +1.10 \\ -0.70 \end{array} \right.$
SLT Tagging Efficiency	$+8, -11$	
Tag Matrix Prediction	± 10	± 0.68
QCD Prediction	± 19 (e) ± 67 (μ)	± 0.14
Drell-Yan and other MC backgrounds	± 19	± 0.05
Luminosity	± 6	± 0.32
Total Systematic Uncertainty		$^{+1.3}_{-1.0}$

VII. RESULTS

Table VI shows a summary of the background estimates and the number of SLT tagged events as a function of the number of jets. A "tagged event" is an event with at least one tagged jet. The total background and the $t\bar{t}$ expectation are also listed. The line labeled "Corrected Background" corresponds to the background after correcting for the $t\bar{t}$ content of the pretagged sample, as described in Section IV A.

TABLE VI: Number of tagged events and the background summary. The $H_{\rm T} > 200$ GeV requirement is made only for events with at least 3 jets.

Background	W + 1 jet	W + 2 jets	W + 3 jets	W + $\geq$ 4 jets	W + $\geq$ 3 jets
Pre-tag Events	9117	2170	211	108	319
Fake, $Wb\bar{b}$, $Wc\bar{c}$, Wc	116.3±11.6	40.5±4.1	7.0±0.7	4.3±0.4	11.3±1.1
WW, WZ, ZZ, $Z \to \tau^+\tau^-$	1.10±0.17	1.33±0.06	0.16±0.02	0.04±0.01	0.19±0.02
QCD	19.6±24.2	12.4±3.5	0.9±0.2	0.8±0.2	1.6±0.3
Drell-Yan	0.8±0.4	0.36±0.20	0.08±0.09	0.00±0.09	0.08±0.09
Single Top	0.50±0.03	0.94±0.06	0.15±0.01	0.035±0.003	0.19±0.01
Total Background	138.2±26.8	55.5±5.4	8.2±0.8	5.2±0.5	13.4±1.3
Corrected Background			9.5±1.1		9.5±1.1
$t\bar{t}$ Expectation (6.7pb)	0.4±0.1	2.9±0.5	5.4±0.9	7.9±1.7	13.3±2.6
Total Background plus $t\bar{t}$	138.6±26.8	58.4±5.4	22.8±2.8		22.8±2.8
Tagged Events	139	48	13	7	20

We calculate the cross section as:

$$\sigma_{t\bar{t}} = \frac{N_{\rm obs} - N_{\rm bgnd}}{A_{t\bar{t}} \cdot \int \mathcal{L} dt}, \tag{9}$$

where $N_{\rm obs}$ is the number of events with ≥ 3 jets that are tagged with at least 1 SLT, $N_{\rm bgnd}$ is the corrected background and $A_{t\bar{t}}$ is the total acceptance (geometrical acceptance times kinematic acceptance times tagging efficiency), taken from Tables III and IV. For events with three or more jets, the total denominator is 1.98 ± 0.28 pb^{-1}.

From the number of candidate events with three or more jets, we find a total $t\bar{t}$ production cross section of

$$\sigma(p\bar{p} \to t\bar{t}) = 5.3 \pm 3.3\ ^{+1.3}_{-1.0}\ \text{pb},$$

where the first uncertainty is statistical and the second is systematic. This cross section value uses acceptances and tagging efficiencies appropriate for a top mass of 175 GeV/c^2. The acceptances and efficiencies, and therefore the calculated cross section, change slightly for other assumed top masses. The calculated cross section is 1% higher assuming a top mass of 170 GeV/c^2, and 5% lower assuming a top mass of 180 GeV/c^2.

Figure 14 shows the number of tags in $W+1, 2, 3, \geq 4$ jet events together with the histograms representing the total corrected background with and without the $t\bar{t}$ signal expectation, based on the theoretical cross section of 6.7 pb for $M_{\rm top} = 175$ GeV/c^2.

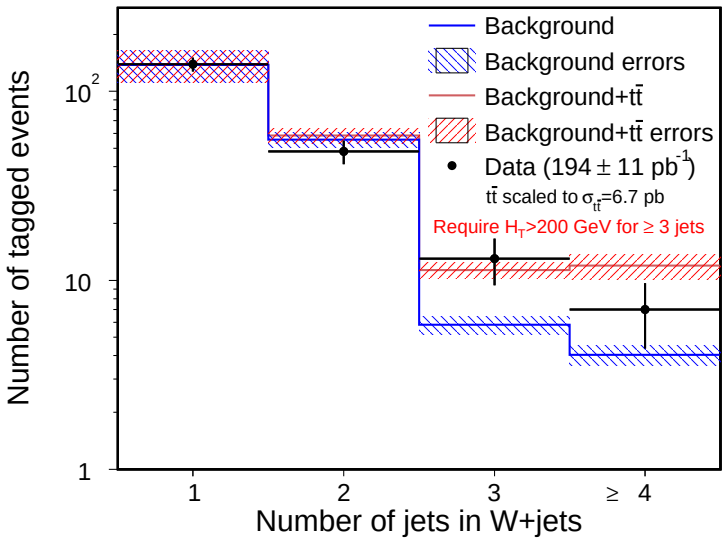

FIG. 14: The expected background and observed tags in $W+$ 1, 2, 3 and 4 or more jet events. The background is corrected for the $t\bar{t}$ content of the pretagged sample.

We examine a number of kinematic distributions of the tagged events and compare with expectations based on the measured signal plus background. Figure 15 shows the $E_{\rm T}$ distribution of the tagged jets in $W+1$ and 2 jets (combined), and in the signal region of W plus three or more jets. The $W+1$ and 2 jet data-Monte Carlo comparison has a Kolmogorov-Smirnov test (KS) probability of 41%, and the three or more jet comparison has a KS probability of 82%.

Figure 16 compares the $P_{\rm T}$ distribution of muons identified as SLT tags with expectations from $t\bar{t}$ plus backgrounds. The KS probabilities are 6% for $W+1$ and 2 jet comparison and 5% for the three or more jet comparison.

Finally, Figure 17 shows the impact parameter significance, defined as the impact parameter divided by its uncertainty, for the SLT tracks and the expectation from signal plus background. The sign of the impact parameter is defined according to whether the track trajectory crosses the jet axis in front of or behind the event primary vertex. The long-lived component from semi-leptonic b-hadron decays is readily apparent in the shape of the positive impact parameter distribution. The KS probabilities are 12% for $W+1$ and 2 jet comparison and 23% for the three or more jet comparison. (Note that Figures 15, 16 and 17 contain 21 entries since one of the events has two jets tagged with SLT.)

VIII. CONCLUSIONS

We have measured the total cross section for $t\bar{t}$ production through the decay of top pairs into an electron or muon plus multiple jets. We separate signal from background by identifying semileptonic decays of b hadrons into muons. The measured $t\bar{t}$ production cross section is $5.3 \pm 3.3^{+1.3}_{-1.0}$ pb, consistent with the expectation of 6.7 pb for standard model production and decay of top quark pairs with a mass of 175 GeV/c^2. Distributions of Jet $E_{\rm T}$ and impact parameter significance for the tagged events, and the distributions of the $P_{\rm T}$ of the tags, are also consistent with standard model expectations.

The sensitivity of this analysis to test non-standard model $t\bar{t}$ production or decay mechanisms is limited by the statistical uncertainty. The combination of this measurement with other CDF II measurements [8] will yield a

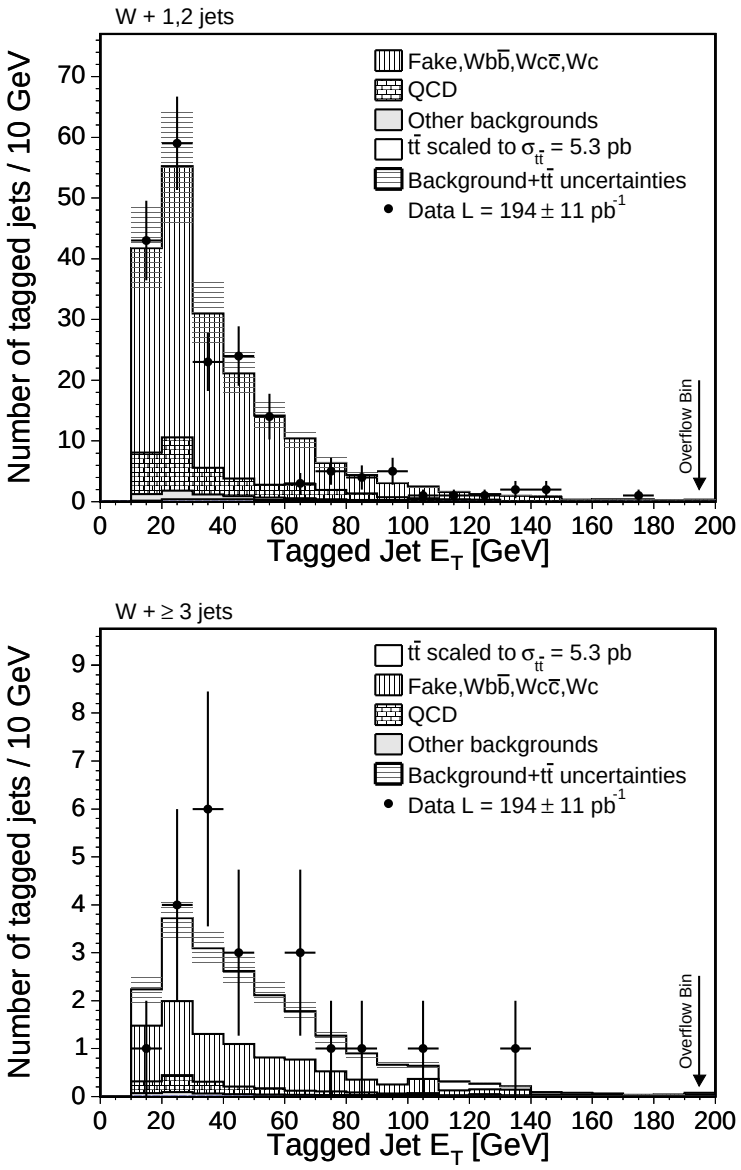

FIG. 15: Comparison of the jet $E_{\rm T}$ distributions for tagged events and for expectations from fakes, QCD and $t\bar{t}$ events. The upper plot is for W+1 and 2 jet events and the lower plot for $W+ \geq 3$ jet events.

significantly more precise value. Future measurements with the full Run II dataset of $4-8$ fb^{-1} will provide further factors of approximately four to six in statistical precision. At the same time, significantly larger datasets will provide avenues for reduction of the systematic uncertainties through such things as better understanding of the tag rate in W+jets events and direct measurement of the tagging efficiency for semileptonic b-hadron decays.

IX. ACKNOWLEDGMENTS

We are grateful to Tim Stelzer for help with studies of the heavy flavor content of γ+jets and W+jets events using `MADEVENT`. We thank the Fermilab staff and the technical staffs of the participating institutions for their vital contributions. This work was supported by the U.S. Department of Energy and National Science Foundation; the Italian Istituto Nazionale di Fisica Nucleare; the Ministry of Education, Culture, Sports, Science and Technology of Japan; the Natural Sciences and Engineering Research Council of Canada; the National Science Council of the Republic of China; the Swiss National Science Foundation; the A.P. Sloan Foundation; the Bundesministerium für Bildung und

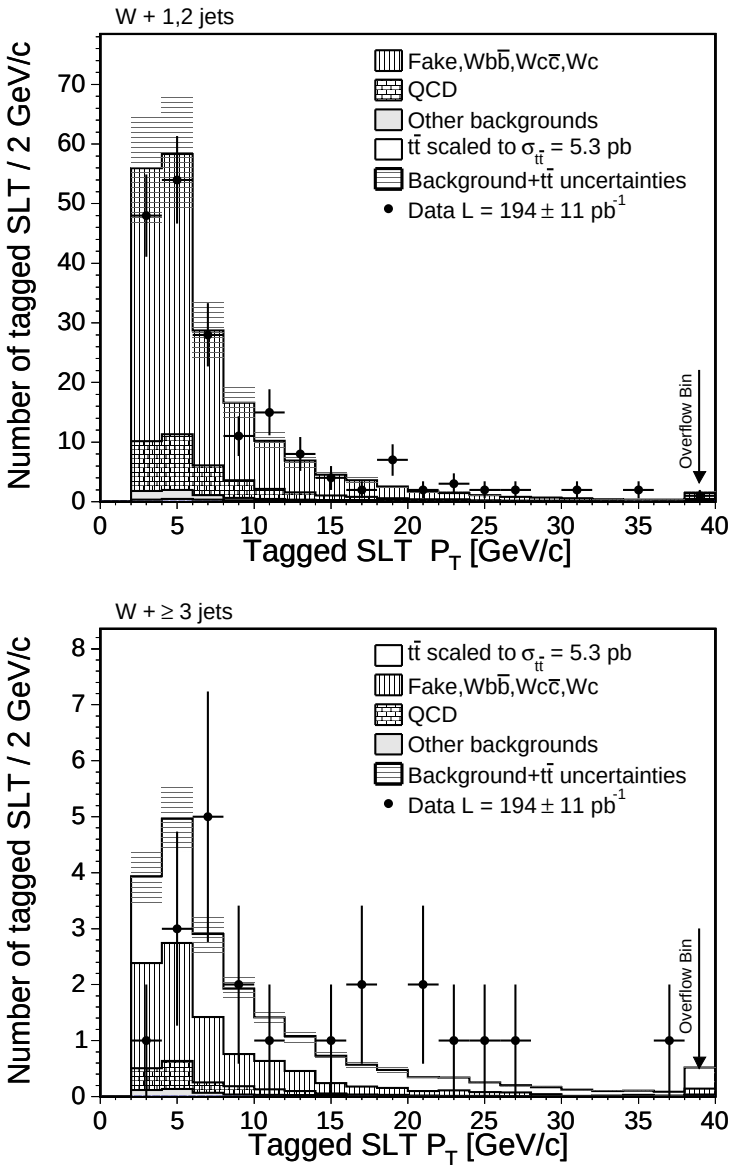

FIG. 16: P_T of the SLT tags. The upper plot is for W+1 and 2 jet events and the lower plot for $W+ \geq 3$ jet events.

Forschung, Germany; the Korean Science and Engineering Foundation and the Korean Research Foundation; the Particle Physics and Astronomy Research Council and the Royal Society, UK; the Russian Foundation for Basic Research; the Comision Interministerial de Ciencia y Tecnologia, Spain; and in part by the European Community's Human Potential Programme under contract HPRN-CT-2002-00292, Probe for New Physics.

[1] M. Cacciari, S. Frixione, G. Ridolfi, M. Mangano and P. Nason, JHEP **404**, 68 (2004); N. Kidonakis and R. Vogt, Phys. Rev. D **68**, 114014 (2003).
[2] C.T. Hill and S.J. Parke, Phys. Rev. D **49**, 4454 (1994).
[3] H.P. Nilles, Phys. Rep. **110**, 1 (1984); H.E. Haber and G.L. Kane, *ibid* **117**, 75 (1985).
[4] We use a (z, ϕ, θ) coordinate system where the z-axis is in the direction of the proton beam, and ϕ and θ are the azimuthal and polar angles respectively. The pseudo-rapidity, η, is defined as $-\ln(\tan\frac{\theta}{2})$. The transverse momentum of a charged particle is $P_{\rm T} = P\sin\theta$, where P represents the measured momentum of the charged-particle track. The analogous quantity

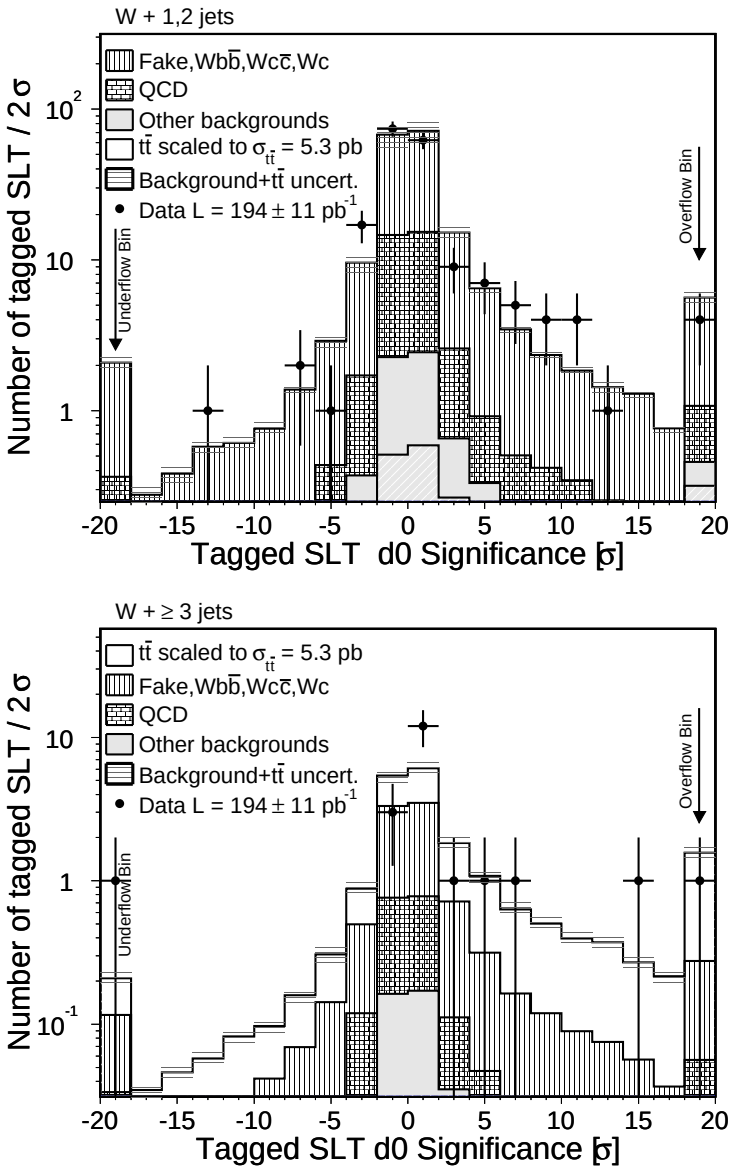

FIG. 17: The impact parameter (d0) significance for tagged events, compared with expectations from backgrounds plus $t\bar{t}$. The upper plot is for W+1 and 2 jet events and the lower plot for $W+ \geq 3$ jet events.

using calorimeter energies, defined as $E_T = E \sin\theta$, is called transverse energy. The missing transverse energy is defined as $\not\!\!E_T = - \mid \sum_i E_T^i \hat{n}_i \mid$ where E_T^i is the magnitude of the transverse energy contained in each calorimeter tower i in the pseudo-rapidity region $|\eta| < 3.6$ and $\hat{n}_i$ is the direction unit vector of the tower in the plane transverse to the beam direction.

[5] D. Acosta *et al.*, Phys. Rev. D **71**, 052003 (2005).
[6] D. Acosta *et al.*, arXiv:hep-ex/0504053. Submitted to Phys. Rev. D.
[7] D. Acosta *et al.* Phys. Rev. D **71** 072005 (2005).
[8] D. Acosta *et al.* To be submitted to Phys. Rev. Lett.
[9] T. Affolder *et al.*, Phys. Rev. D **64**, 032002 (2001); V.M. Abazov *et al.*, Phys. Rev. D **67**, 012004 (2003).
[10] The CDF II Detector Technical Design Report, Fermilab-Pub-96/390-E ; D. Acosta *et al.*, Phys. Rev. **D71**, 032001 (2005).
[11] S. Klimenko, J. Konigsberg and T.M. Liss, Fermilab-FN-0741.
[12] D. Acosta *et al.*, Inclusive W and Z Cross Sections from Run II of the Tevatron Collider, to be submitted to Phys. Rev. D .
[13] T. Sjostrand *et al.*, Comput. Phys. Commun. **135**, 238 (2001).
[14] G. Corcella *et al.*, JHEP **01**, 10 (2001).

[15] J. Pumplin, *et al.*, Eur. Phys. J. **C12**, 375 (2000).
[16] P. Avery, K. Read and G. Trahern, CLEO Report CSN-212 (1985). Unpublished.
[17] M. Mangano *et al.*, JHEP **07**, 001 (2003).
[18] R. Brun and F. Carminati, CERN Programming Library Long Writeup **W5013** (1993).
[19] T. Affolder *et al.*, Nucl. Instrum. and Methods A **526**, 249 (2004).
[20] G. Grindhammer, M. Rudowicz and S. Peters, Nucl. Instrum. and Methods A **290**, 469 (1990).
[21] E. Gerchtein and M. Paulini, ECONF **C0303241**, TUMT005 (2003), arXiv:physics/0306031.
[22] F. Maltoni and T. Stelzer, `MADEVENT:` Automatic Event Generation with `MADGRAPH`, JHEP 0302:027 (2003).
[23] J. Campbell and R. Ellis, Phys. Rev. D **60**, 113006 (1999).
[24] D. Acosta *et al.*, Phys. Rev. Lett. **94**, 091803 (2005).
[25] B. Harris, E. Laenen, L. Phaf, Z. Sullivan and S. Weinzierl, Phys. Rev. D **66**, 054024 (2002).
[26] D. Acosta *et al.*, FERMILAB-PUB-04-370-E. Submitted to Phys. Rev. D.